

Open Research Online

The Open University's repository of research publications
and other research outputs

AKARI/IRC source catalogues and source counts for the IRAC Dark Field, ELAIS North and the *AKARI* Deep Field South

Journal Item

How to cite:

Davidge, H.; Serjeant, S.; Pearson, Chris; Matsuhara, H.; Wada, T.; Dryer, B. and Barrufet, L. (2017). *AKARI*/IRC source catalogues and source counts for the IRAC Dark Field, ELAIS North and the *AKARI* Deep Field South. *Monthly Notices of the Royal Astronomical Society*, 472(4) pp. 4259–4286.

For guidance on citations see [FAQs](#).

© 2017 The Authors

Version: Version of Record

Link(s) to article on publisher's website:
<http://dx.doi.org/doi:10.1093/mnras/stx1935>

Copyright and Moral Rights for the articles on this site are retained by the individual authors and/or other copyright owners. For more information on Open Research Online's data [policy](#) on reuse of materials please consult the policies page.

oro.open.ac.uk

AKARI/IRC source catalogues and source counts for the IRAC Dark Field, ELAIS North and the AKARI Deep Field South

H. Davidge,^{1★} S. Serjeant,¹ C. Pearson,^{1,2,3} H. Matsuhara,^{4,5} T. Wada,⁴ B. Dryer¹ and L. Barrufet^{1,2}

¹*School of Physical Sciences, The Open University, Milton Keynes, MK7 6AA, UK*

²*RAL Space, Rutherford Appleton Laboratory, Chilton, Didcot, Oxfordshire OX11 0QX, UK*

³*Oxford Astrophysics, Denys Wilkinson Building, University of Oxford, Keble Rd, Oxford OX1 3RH, UK*

⁴*Institute of Space and Astronautical Science, Japan Aerospace Exploration Agency, Sagami-hara, Kanagawa 229-8510, Japan*

⁵*Department of Space and Astronautical Science, The Graduate University for Advanced Studies, Hayama, Kanagawa 240-0193, Japan*

Accepted 2017 July 26. Received 2017 July 25; in original form 2017 May 25

ABSTRACT

We present the first detailed analysis of three extragalactic fields (IRAC Dark Field, ELAIS-N1, ADF-S) observed by the infrared satellite, *AKARI*, using an optimized data analysis toolkit specifically for the processing of extragalactic point sources. The InfaRed Camera (IRC) on *AKARI* complements the *Spitzer Space Telescope* via its comprehensive coverage between 8–24 μm filling the gap between the *Spitzer*/IRAC and MIPS instruments. Source counts in the *AKARI* bands at 3.2, 4.1, 7, 11, 15 and 18 μm are presented. At near-infrared wavelengths, our source counts are consistent with counts made in other *AKARI* fields and in general with *Spitzer*/IRAC (except at 3.2 μm where our counts lie above). In the mid-infrared (11–18 μm), we find our counts are consistent with both previous surveys by *AKARI* and the *Spitzer* peak-up imaging survey with the InfraRed Spectrograph (IRS). Using our counts to constrain contemporary evolutionary models, we find that although the models and counts are in agreement at mid-infrared wavelengths there are inconsistencies at wavelengths shortward of 7 μm , suggesting either a problem with stellar subtraction or indicating the need for refinement of the stellar population models. We have also investigated the *AKARI*/IRC filters, and find an active galactic nucleus selection criteria out to $z < 2$ on the basis of *AKARI* 4.1, 11, 15 and 18 μm colours.

Key words: methods data analysis – catalogues – surveys – infrared: galaxies.

1 INTRODUCTION

One of the most basic statistical properties in the analysis of galaxy populations is galaxy source counts. Originally suggested as a method of determining the geometry of the Universe, early discoveries using the results from counts at radio wavelengths showed that the Universe is inconsistent with a steady-state model (Rowan-Robinson 1967). Subsequently galaxy source counts have been used to study galaxy evolution, star formation history and the epoch of galaxy formation (e.g. Ellis 1987).

Given that around half of the energy in the Universe is emitted at infrared wavelengths, models of infrared galaxy counts have become important in analysing the dusty star-formation history of the Universe (Franceschini et al. 1991; Blain & Longair 1993; Pearson & Rowan-Robinson 1996). One key infrared wavelength

regime to study galaxy evolution is the mid-infrared, as this probes the polycyclic aromatic hydrocarbon (PAH), silicate feature and active galactic nucleus (AGN) emission as a function of redshift. Large area multiwavelength surveys have been carried out by *Spitzer* (Werner et al. 2004), *AKARI* (Murakami et al. 2007) and *WISE* (Wright et al. 2010).

AKARI was Japan's first satellite dedicated to infrared astronomy; launched on 2006 February 21, it was operational until 2011 November 24 (Murakami et al. 2007). *AKARI* carried a Ritchey-Chrétien telescope, with effective diameter of 68.5 cm, and two instruments: Far-Infrared Surveyor (FIS; Kawada et al. 2007) observing from 50 to 180 μm and the InfraRed Camera (IRC; Onaka et al. 2007) observing at 1.5–26.5 μm .

The *AKARI* archive has over 5000 individual observations and contains multiple pointings of many extragalactic deep fields. The *AKARI*/IRC imaging covers the 8–24 μm band gap between *Spitzer*/MIPS and *Spitzer*/IRAC, and is able to observe deeper

* E-mail: helen.davidge@open.ac.uk

Table 1. Specifications of the nine filters in the IRC.

Channel	Name	Filter	Wavelength (μm)	Centre (μm)	Effective width (μm)	Detector	Array size (pixels)	Imaging FoV (arcmin)	Pixel scale (arcsec)
NIR	N2	filter	1.9–2.8	2.34	0.71	InSb	512×412	9.3×10.0	1.46×1.46
NIR	N3	filter	2.7–3.8	3.19	0.87	InSb	512×412	9.3×10.0	1.46×1.46
NIR	N4	filter	3.6–5.3	4.33	1.53	InSb	512×412	9.3×10.0	1.46×1.46
MIR-S	S7	filter	5.9–8.4	7.12	1.75	Si:As	256×256	9.1×10.0	2.34×2.34
MIR-S	S9W	filter	6.7–11.6	8.61	4.10	Si:As	256×256	9.1×10.0	2.34×2.34
MIR-S	S11	filter	8.5–13.1	10.45	4.12	Si:As	256×256	9.1×10.0	2.34×2.34
MIR-L	L15	filter	12.6–19.4	15.58	5.98	Si:As	256×256	10.3×10.2	2.51×2.39
MIR-L	L18W	filter	13.9–25.6	18.39	9.97	Si:As	256×256	10.3×10.2	2.51×2.39
MIR-L	L24	filter	20.3–26.5	22.89	5.34	Si:As	256×256	10.3×10.2	2.51×2.39

over this wavelength range than any other telescope (Werner et al. 2004).

In this paper, we present an optimized data processing chain for *AKARI*/IRC data, specifically tailored for the production of high-quality extragalactic images and the extraction of galaxy point sources. In Section 2, we review the original and new archival pipelines in the context of the IRC instrument and the *AKARI* mission. In Section 3, the new optimized toolkit is described, step by step. In Section 4, the optimized toolkit is applied to a deep early- to mid-Phase 2 data (Section 4.1), deep late-Phase 2 data (Section 4.2) and a shallow (Section 4.3) field, respectively. Our results, including the galaxy source counts are presented in Section 5 and discussed in the wider context of observational galaxy surveys and phenomenological source count models in Section 6. The *AKARI*/IRC colour–colour space is explored, with the view to find an AGN selection criteria. Finally, our conclusions are presented in Section 8. Throughout this work, we assume a concordance cosmology of a Hubble constant of $H_0 = 67.8 \text{ km s}^{-1} \text{ Mpc}^{-1}$ and density parameters of $\Omega_M = 0.3$ and $\Omega_\Lambda = 0.7$.

2 THE IRC INSTRUMENT AND PIPELINE

2.1 Instrumentation

The IRC contained three detectors, the NIR (near-infrared), the MIR-S (mid-infrared short) and the MIR-L (mid-infrared long), each of which had three filters and one prism or grism. The imaging area is smaller than the array, because the area of the array around the slit was masked. The NIR and MIR-S detectors share the same field of view (FoV); the FoV of the MIR-L detector is offset by ~ 20 arcmin. The imaging specifications of the nine *AKARI*/IRC filters are presented in Table 1. These specifications did not alter during the mission.

The *AKARI* mission was divided into three phases. In Phase 1, from 2006 May to 2006 November, *AKARI* performed an All-Sky Survey at far-infrared (Yamamura et al. 2010) and mid-infrared (Ishihara et al. 2010) wavelengths. Phase 2 spanned 2006 November to 2007 August and was predominantly populated by guaranteed time observations (referred to as Mission Programmes) and Open Time observations. During Phases 1 and 2, the telescope and instruments, including the IRC, were cryogenically cooled to $\sim 6 \text{ K}$. The supply of liquid helium coolant was exhausted in 2007 August. A warm Phase 3 operating only the NIR detector at 40 K , consisted mainly of Open Time observations (Murakami et al. 2007).

2.2 The original archival pipeline

The original archival IRC imaging pipeline (version 20110304) used to populate the *AKARI* data archive runs in the IRAF¹ environment. The original archival pipeline was written to process all of the *AKARI*/IRC pointings, both Galactic and extragalactic. The original archival pipeline is sub-divided into three parts: the pre-pipeline, the pipeline and the post-pipeline. The pre-pipeline slices the raw 3D data cubes into 2D image frames and creates an observation log file for use in subsequent steps. The main pipeline is comprised of 11 processing steps, which correct for numerous instrumental artefacts, perform dark subtraction and flat-fielding. The post-pipeline has four steps to coadd the individual frames from each pointing together and a step to correct for any offset in the applied World Coordinate System (WCS; Lorente et al. 2007).

There were several outstanding issues with the original archival IRC pipeline that prompted the development of the reanalysis in this paper, and in parallel drove some of the changes to the instrument team’s IRC pipeline (itself informed in part by the work in this paper), discussed in the next section. The raw frames suffer from an astrometry error; to be aligned with the correct WCS, each frame needs to be astrometry corrected. The new and updated archival pipeline (discussed below) makes a partial correction for this error. The raw IRC frames are also warped; this warping is due to both an optical distortion and because the detectors are not completely square on the sky. Frames from several of the IRC filters can also remain badly affected by reflected Earthshine light that creates a flux gradient across the frame. The original archival pipeline also only makes partial corrections for the image warping and the Earthshine gradient artefact.

2.3 Updated archival pipeline

There exists a major improvement to the original archival pipeline. This new archival pipeline is discussed in detail in Egusa et al. (2016). This updated pipeline was written to process all IRC pointings taking during Phases 1 and 2, totalling ~ 4000 pointings. All the pointings have been processed through this new archival pipeline and are available for public download from the *AKARI* archive. The new archival pipeline has done much work on the dark and flat-field corrections, but has not corrected for several artefacts, including *column pull-down*, *muxbleed* (both discussed below), ‘ghosts’, memory effects and Earthshine light. For fields with enough sources, the new archival pipeline has been able to perform an astrometry correction.

¹ IRAF is distributed by the National Optical Astronomy Observatory, which is operated by the Association of Universities for Research in Astronomy, Inc., under cooperative agreement with the National Science Foundation.

It should be noted that the new archival pipeline is written to process generic IRC observations, both Galactic and extragalactic, and hence is not optimized for the specific processing of extragalactic images for point source extraction, which is the specific objective of this work.

3 THE OPTIMIZED TOOLKIT

3.1 Overview

This paper presents a new toolkit (hereafter referred to as the optimized toolkit) for the specific use of processing extragalactic *AKARI* deep-field images that the archival pipelines were unable to do to a high enough scientific level. The optimized toolkit was written in the INTERACTIVE DATA LANGUAGE (IDL),² in order to take advantage of IDL's array based processing, which is well suited to the IRC data sets. This new toolkit has been created with the assistance of the *AKARI*/IRC archival team.

The raw *AKARI* data are accessed as individual pointings from the archive, consisting of 3D data cubes. The raw 3D data cubes are sliced into 2D frames using the original archival pre-pipeline. The first step of the optimized toolkit creates a structure to hold the frame, associated header, noise array, noise header, mask array and mask header. Neither archival pipelines create a mask or noise image from each frame. In order to ensure that the optimized toolkit is efficient and to avoid excessive reading and writing to/from storage, all frames are passed as IDL structures between processing steps. The subsequent steps of the optimized toolkit are shown in Fig. 1.

It should be noted that the dark current subtraction, the normalization, linearity correction, anomalous pixels and flat-fielding steps of the optimized toolkit, see dashed boxes in Fig. 1, replicate the same steps in the original archival pipeline. The new archival pipeline uses the dark subtraction method from Tsumura & Wada (2011), using time-dependent dark frames for each pointing. This optimized toolkit also uses time-dependent dark frames, selected from suitable pointings over the entire Phase 2 period. The normalization steps correct for data compression and Fowler sampling. The linearity step corrects for a non-linear relationship between the number of electrons and analogue-to-digital unit (ADU; Lorente et al. 2007).

The optimized toolkit modules are described in turn below.

3.2 Wraparound correction

Due to telemetry constraints on the data size for downlink, data were compressed on board; all pixels with a flux greater than 2^{16} ADUs are 'wrapped around' to a pixel value less than -11953.8 ADU (Lorente et al. 2007). Fig. 2 shows examples of artefacts created by a bright (many times brighter than the detector full well) object (star, cosmic ray, etc.) viewed by the detector. There are two clear effects: every fourth pixel after the pixel that the bright object is incident on shows a brighter value; and the column in which the bright object pixel is situated also shows an increase in signal. The first effect, termed *muxbleed*, is understood to be due to the extreme signal charge not being completely reset from the output chain, resulting in an offset applied to subsequent reads from that output (of which there are four between those pixels that are multiplexed) for some time until the offending signal has decayed in the electronics. The

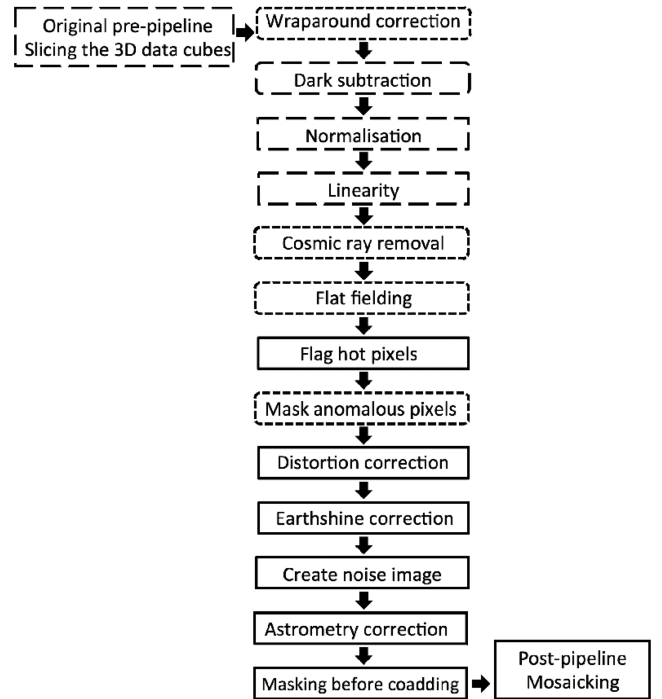


Figure 1. Outline of the steps in the optimized toolkit. The dashed line boxes are steps copied directly from the original archival pipeline. The dotted line boxes are based on steps from the original archival pipeline, with some changes, e.g. a more comprehensive masking in the wraparound correction, cosmic ray and mask anomalous pixels steps, and incorporating a time-dependent flat-field. The solid line boxes are steps created for the optimized toolkit.

second effect, often referred to as *column pull-down*, is likely to be a blooming effect during the integration time. Blooming is when a large number of photons (or signal from a very high energy photon) fills the full well capacity of the pixel it is incident on. The electron signal then blooms to the next pixel and so on, until all the electrons have been captured in potential wells.

Column pull-down and *muxbleed* are not corrected for in either the original or new archival pipelines. This optimized toolkit masks the affected pixels, similar to Murata et al. (2013). In the paper of Murata et al. (2013), all columns with *Column pull-down* and rows with *muxbleed* are masked. All columns affected by *Column pull-down* are masked, but only every fourth pixel in rows affected by *muxbleed* are masked. This is performed by the optimized toolkit by first checking each NIR frame for pixels with a value less than -11953.8 ADU. The location of the pixel is flagged in the mask image, as are all the pixels in the same column (affected by the *column pull-down* effect) and every fourth pixel for the following two rows (due to the *muxbleed* effect).

During the work of creating the optimized toolkit, a new artefact in many of the NIR images was discovered. The artefact is a pattern, with sets of four pixels with increased flux and decreased flux, as shown in Fig. 3. This is not mentioned in the archival pipelines or previous toolkits. As the pattern is in sets of four, it is presumed to be linked to reset changing of the four read-out nodes. A limitation of the optimized toolkit is that it does not remove this artefact. Further work is required to research how to remove this new artefact.

² INTERACTIVE DATA LANGUAGE: <http://www.exelisvis.com/ProductsServices/IDL.aspx>

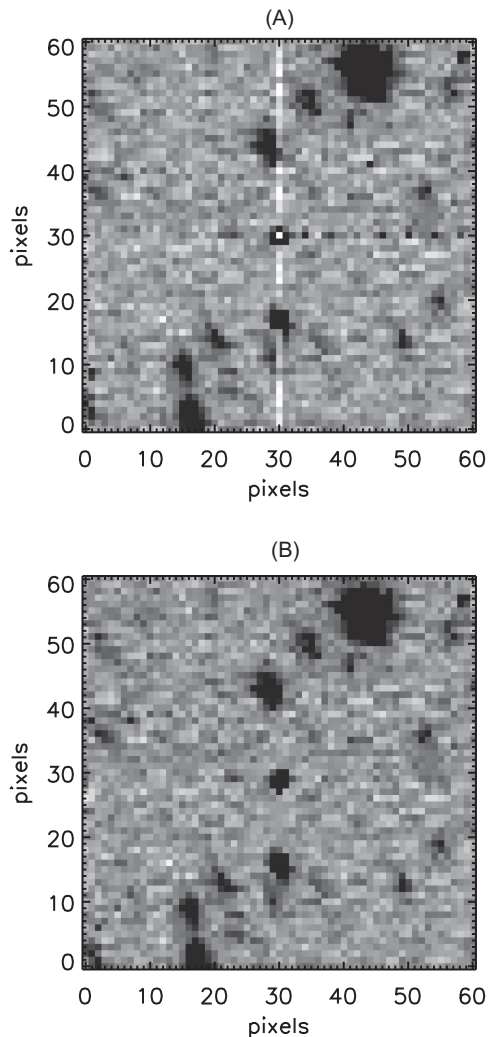


Figure 2. A close-up of a single N3 frame: image (a) shows the raw frame and image (b) shows the processed frame with muxbleed removed. The saturated pixel causing the artefact is at pixel number (30, 30). The masked pixels have been assigned an interpolated value.

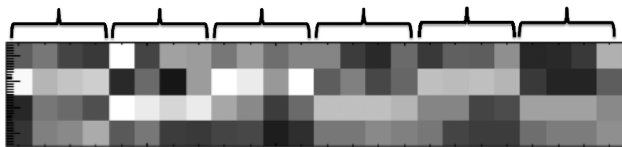


Figure 3. Close-up of an NIR frame, showing the sets of four pixels and the increasing and decreasing flux.

3.3 Cosmic ray removal

Frames from all of the nine filters contain cosmic rays. The cosmic ray detection was found not to work well in the original archival pipeline, and is not mentioned in the new archival pipeline. The optimized toolkit detects cosmic rays in two places, in the cosmic ray detection step (i.e. in individual frames) and additionally during the later coadding stage. Quite often, the first NIR frame in a pointing contains many more cosmic rays than subsequent frames. This is due to the detector not being read out between pointings causing build-up of cosmic ray signals. The IDL procedure `LA_COSMIC` (van Dokkum 2001), an algorithm to detect cosmic rays using Laplacian

edge detection, is used to remove the cosmic rays in the individual NIR frames.

In the MIR-S and -L bands, the cosmic rays appear very similar to faint point sources and `LA_COSMIC` was found to remove some of the point sources as well. In order to preserve the flux from the point sources, in the cosmic ray removal step for the MIR-S and -L bands, a simple source extraction algorithm was run on the individual frames to detect connected pixels. The threshold was set low, so as to mask as many point sources as possible. Each frame with the connected pixels masked, was then put through a sigma clipping algorithm to detect spuriously bright single pixels. The algorithm was written for the optimized toolkit. A different sigma level was used for each detector. Before the implementation of the masking of connected pixels, flux was lost from point sources. The masking of the connected pixels minimizes the loss of flux. The locations of detected cosmic rays are flagged in the array mask. A second cosmic ray detection is performed during the frame coadding stage. This is mainly performed to detect any remaining cosmic rays that were incorrectly masked as point sources. The same sigma clipping algorithm is performed in the coadding stage.

3.4 Flat-fielding

The optimized toolkit creates a bespoke flat, using frames time-stamped with a similar date to the observation. To remove as many instrumental artefacts as possible, we have found it advisable to create time-dependent flats for each date range of a set of pointings. One prominent artefact removed by such a bespoke flat-field is the so-called *sora-mame* (Japanese for sky-bean due to the artefact's shape, hereafter called 'the bean'). The bean appears in MIR-S detector images from the beginning of the mission to part way through Phase 2, where it disappeared on 07/01/2007. The bean is a pattern of three almost circular shapes (see Fig. 4a). The shape of the bean is time dependent, and there is currently no generic model to remove it. The time-dependent flats created for use with the new archival pipeline were found not to remove the bean in the frames processed in Section 4. Following the method outlined in Murata et al. (2013), a very time-dependent bespoke flat (of order of a couple of days) was found to remove the bean. Comparison between the use of the generic flat-field and a bespoke time-dependent flat-field can be seen in Fig. 4.

3.5 Flag hot pixels

Analysis of images from the IRC shows that there is an increase in the number of hot/bright pixels over the duration of the mission. These hot pixels are visible in frames as having a high dark current. This is likely to have been caused by displacement damage from impacting protons. This damage is ever-more evident in later-Phase 2 MIR-S and MIR-L images. In addition, in the MIR-S detector images there is a spread of hotter pixels in the lower right-hand side of the frame. This is the part of the image nearest to the amplifier, which increases dark current in surrounding pixels. This is worsened by the warming up of the telescope, which gets worse over the mission. This area needs to be masked in later-Phase 2 MIR-S images. Both of these artefacts are evident in the images and a bespoke time-dependent flat is unable to correct for them.

The original hot pixel masks provided by the *AKARI*/IRC instrument team (shown in Figs 5a and b) for use with the original archival pipeline were found not to mask all the hot pixels. Also, the method of hot pixel detection used by the new archival pipeline was found not to work on the pointings processed in Section 4. For this toolkit,

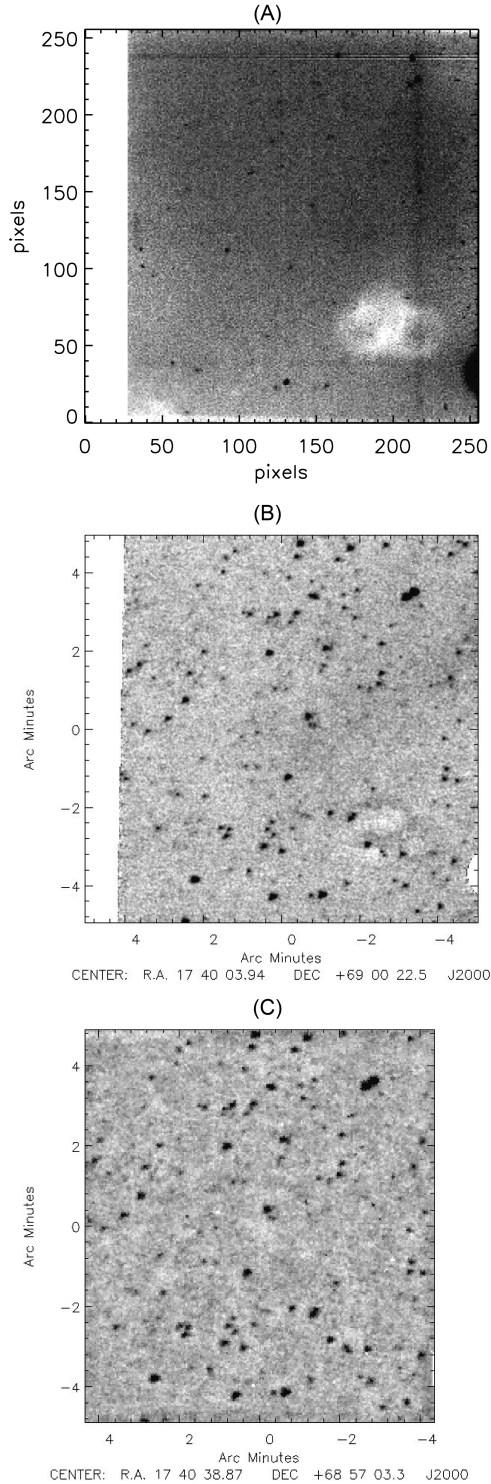


Figure 4. An example of the improvement provided by the optimized toolkit for the bean removal, following the method used in Murata et al. (2013). For reference (a) shows a raw single frame note the sky bean is the white patch in the bottom right. Image (b) shows a single pointing processed by the new archival pipeline (Egusa et al. 2016), note that the bean has not been fully removed. Image (c) shows the same pointing processed by the optimized toolkit, the sky bean has been fully removed. This image has been cropped, so as not to contain the slit area.

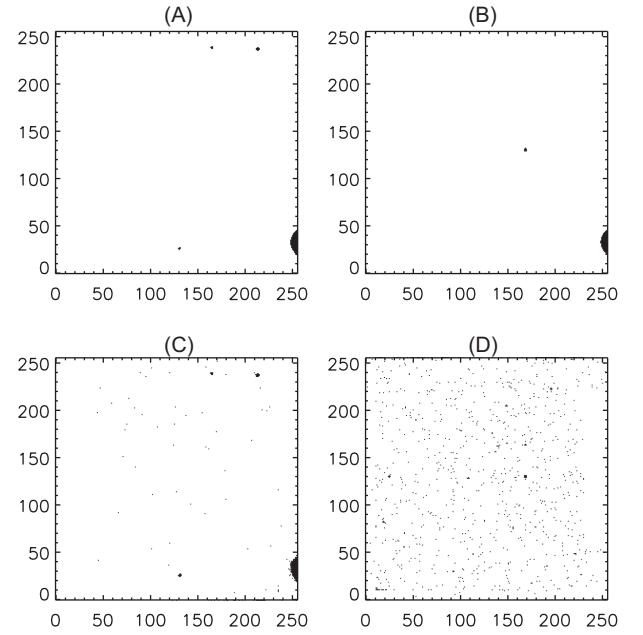


Figure 5. Hot pixel masks: image (a) shows the original MIR-S hot pixel mask and (b) shows the original MIR-L hot pixel mask. Image (c) shows the optimized toolkit hot pixel mask for MIR-S and (d) shows the optimized toolkit hot pixel mask for MIR-L.

a different method was used. The optimized toolkit uses a new template to flag the location of hot pixels in the mask array associated with each image. These new templates to mask the locations of hot pixels in in MIR-S and MIR-L frames are shown in Figs 5c and d. The hot pixels cannot be removed by a time-dependent flat, due to the fact that the background flux of the image varies considerably during a single pointing (see Section 3.8.2). The new hot pixel mask was created from late-Phase 2 *AKARI* observations. Only the first two-thirds of the frames from each pointing were used. The NIR detector does not appear to have the same later-Phase 2 artefacts. Fig. 6 shows the improvement the optimized toolkit does in removing the hot pixels. The figure gives a comparison between a coadded pointing processed by the new archival pipeline suffering from hot pixels, and the same pointing coadded using the optimized pipeline.

3.6 Mask anomalous pixels

In the original archival pipeline, image pixels identified as ‘bad’ are set to -9999.90 ADU, whereas the optimized toolkit flags the locations of bad pixels in the associated mask array. The steps in the optimized toolkit, which flag bad pixels are wraparound correction, cosmic ray removal and mask anomalous pixels. Both archival pipelines also masks the slit area, whereas the optimized toolkit does not, as it contains information about the dark current. The slit area is masked during the coadding stage.

3.7 Distortion correction

The raw *AKARI* data suffer from an image distortion. This distortion depends on the detector (NIR, MIR-S or MIR-L, and to a lesser degree on the filter, see Table 1). Neither archival pipelines discuss the image distortion, and do not correct for it. This distortion is corrected for in the optimized toolkit. To correct for this distortion, true sky positions are obtained using the 2MASS catalogue (Skrutskie et al. 2006) for NIR detector frames and the *WISE*

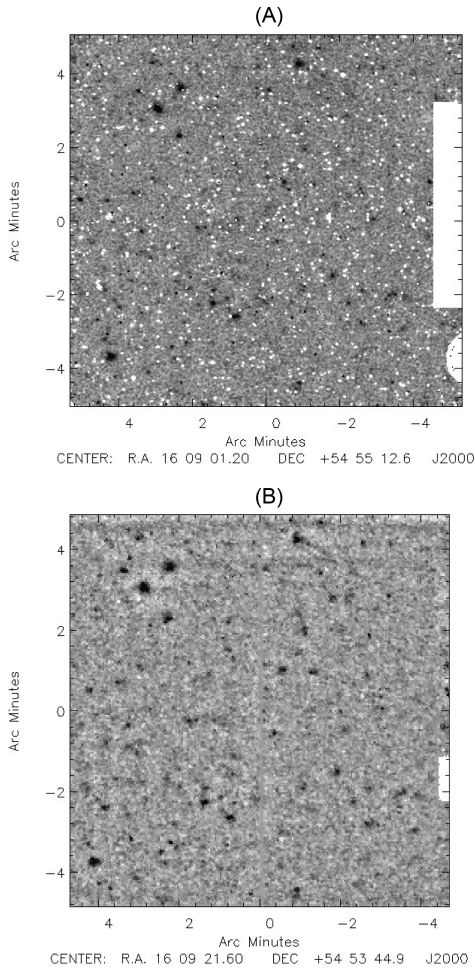


Figure 6. An example of the improvement provided by the optimized toolkit for masking hot pixels. Hot pixels are most evident in late-Phase 2 frames, due to accumulation of radiation damage. Image (a) shows a single pointing processed by the new archival pipeline (Egusa et al. 2016), note the white pixels, which are the hot pixels. Image (b) shows the same pointing processed by the optimized toolkit. This image has been cropped, so as not to contain the slit area.

catalogue (Wright et al. 2010) for the MIR-S and MIR-L frames. Using these *AKARI*/ancillary point source pairs, a χ^2 multiparameter fitting programme (Markwardt 2009) was used to simultaneously fit the distortion polynomial using the astrometry. The distortion correction and the astrometry were then iterated until the χ^2 of the fit of the difference between the *AKARI* positions and 2MASS/WISE positions were at a minimum. Using this method, a second-order polynomial distortion correction was created for each filter:

$$X' = \sum_{i=0}^N \sum_{j=0}^n P_{ij} x^j y^i, \quad (1)$$

$$Y' = \sum_{i=0}^N \sum_{j=0}^n Q_{ij} x^j y^i. \quad (2)$$

The second-order polynomial distortion correction for the x -axis and y -axis are given, respectively, by equations (1) and (2), where x is the original distorted x pixel position, y is the original distorted y pixel position, X' is the undistorted x pixel position, Y' is the undistorted y pixel position, P_{ij} is the x matrix transformation, Q_{ij} is the

y matrix transformation, N is the order of polynomial and n is the square root of the number of elements of the matrix.

The vector plot for the distortion correction for each of the nine filters are shown in Fig. 7 and the distortion polynomial coefficients themselves are listed in the Appendix. The distortion correction polynomials created for the optimized toolkit, used in the processing of the three extragalactic fields discussed in Section 4, have all been found to be accurate to within the Nyquist scale, i.e. less than half of the full-width half maximum (FWHM). Table 2 shows the pixel error for the IRC filters in Section 4.

The above method assumes that for each filter the distortion is not time dependent during Phase 2 of the *AKARI* mission. The distortion correction was tested on frames from 2006 November (early Phase 2), 2007 February (mid Phase 2) and 2007 July (late Phase 2), no time dependence was found. Approximately 20 frames of different extragalactic deep fields were used to create the NIR distortion polynomials. Individual frames of extragalactic deep fields could not be used to create the MIR-S and MIR-L distortion correction polynomials. There are two main reasons for this: first, both raw and processed individual frames do not show many point sources (see Fig. 4a for an example of an individual MIR frame); secondly, in individual frames, point source extraction often incorrectly labels hot pixels as point sources, which would be removed in the coadding stage. For the χ^2 multiparameter fitting to work correctly, each individual frame was required to have 20 + galaxies. Therefore, frames of Galactic targets were used instead for MIR-S and MIR-L images. The distortion correction also automatically corrects the aspect ratio.

3.8 Earthshine correction

3.8.1 Earthshine artefact

IRC frames suffer from Earthshine, caused by sunlight reflected by the Earth on to the telescope. This artefact appears as an area of increased incident flux, which can move around the image from frame to frame. The Earthshine artefact can be seen in images from all of the nine IRC filters. The Earthshine effect is worse in the MIR detector images and also during later-Phase 2 observations. Fig. 8 shows nine individual MIR-S raw frames from a 30 frame single S11 pointing observed during late-Phase 2. The figure clearly shows that the Earthshine artefact moves around the image, from frame to frame, during a single pointing. A template or time-dependent flat is not able to remove this artefact. Neither of the archival pipelines were able to fully remove the Earthshine artefact. Egusa et al. (2016) state that they have a template that is able to remove this artefact when it is fairly low level. The optimized toolkit removes this artefact by creating a boxcar median-filtered image for each frame and subtracts this from the original image. Fig. 9 shows the improvement to a coadded pointing, after the removal of the Earthshine artefact from each individual frame.

3.8.2 Temperature change of the detectors

Present in all observations, over a single pointing the background flux of the detector decreases and then increases. This is worse for pointings taken at later stages of the mission and for MIR-S and MIR-L images. This is due; to the Sun's light warming the telescope, causing the entire detector to change temperature. Fig. 10 shows how much the average sky background flux alters over a single pointing. The flux variation follows the same pattern for different pointings but the magnitude of the effect varies. Neither of

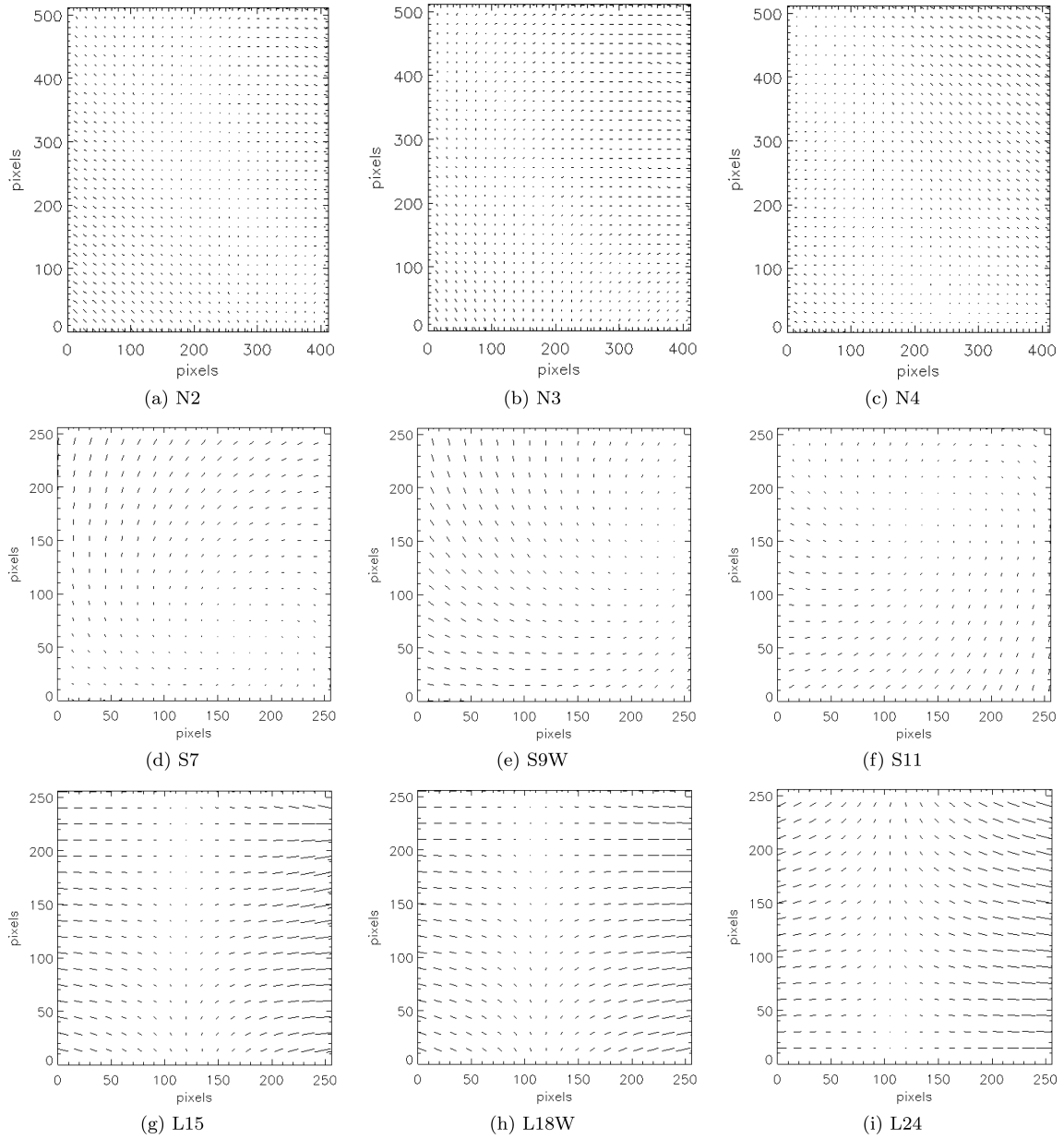


Figure 7. Distortion correction polynomials for the nine filters calculated using equations (1) and (2) and the coefficients in the Appendix.

Table 2. The positional error of the six IRC filters used in Section 4.

Filter	Positional error/pixels
N3	0.42
N4	0.63
S7	0.57
S11	0.69
L15	0.56
L18W	0.59

the archival pipelines discusses this artefact. The optimized toolkit corrects for this, by masking the point sources and calculating the average background flux for each frame. During the coadding stage (Sections 4.1–4.2), the corresponding average value is subtracted from each frame.

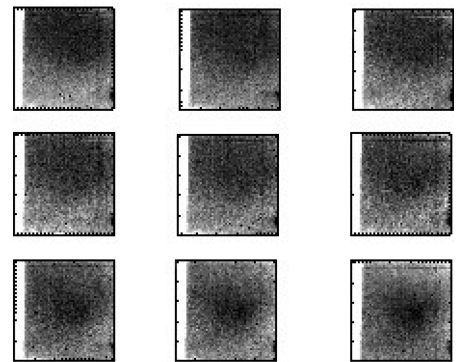


Figure 8. A sample of nine raw frames from one S11 30 frame pointing from later-Phase 2 data. Note how the Earthshine artefact ‘moves’ over the image from frame to frame.

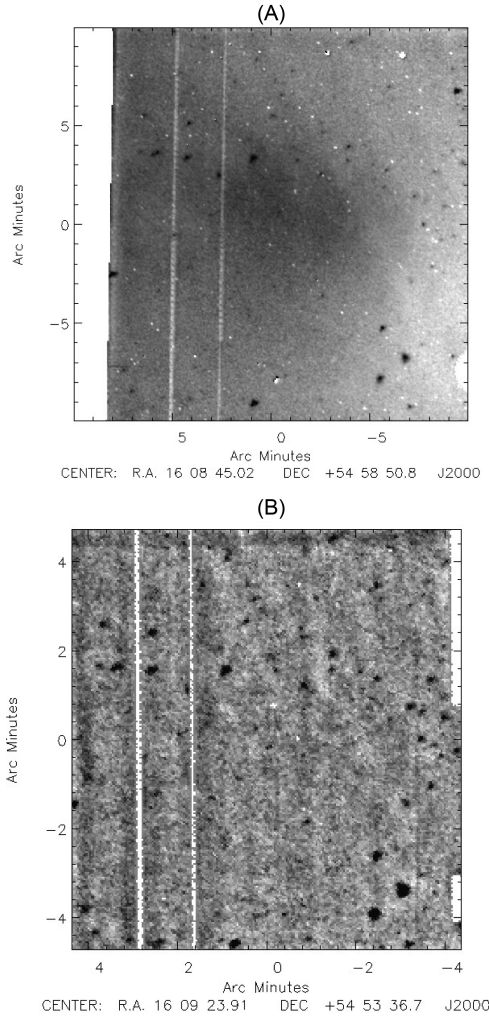


Figure 9. Example of the improvement provided by the optimized toolkit for removal of the Earthshine light. Image (a) shows a single pointing processed by the new archival pipeline (Egusa et al. 2016), with the Earthshine evident as a strong flux effect; Image (b) shows the same pointing processed by the optimized toolkit, with Earthshine light successfully removed. The image has been cropped, so as not to contain the slit area, also the white horizontal lines in image (b) are masked. These lines have not been masked in image (a).

3.8.3 Extended ghosting

The MIR-L detector images suffer an additional artefact, referred to as extended ghosting (see Fig. 11a), caused by light reflecting off the array or filter, on to the detector. This artefact is removed in the same toolkit step as the Earthshine light (see Section 3.8.1), by subtracting a boxcar median-filtered image from the original frame. The removal of this artefact is demonstrated in Fig. 11.

3.9 Create noise image

The optimized toolkit creates a separate noise image for each frame. Neither archival pipelines creates an individual noise image for each frame, but only creates a noise image from each coadded pointing. Individual noise images for each frame are required when performing noise-weighted coadding. The noise value for each pixel is calculated using equation (3) (Mortara & Fowler 1981):

$$N_T = \sqrt{N_* + n_{\text{pix}}(N_S + N_D + N_R^2)}, \quad (3)$$

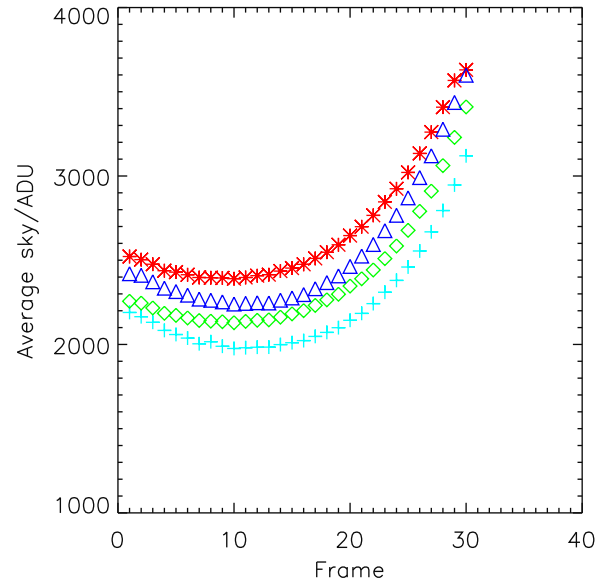


Figure 10. Image showing the change in average background flux of the frames over a pointing. Each different coloured shape represents a different observation.

where N_T is the total noise of the pixel, N_* is derived from the total number of photons, n_{pix} is the number of pixels, in this case $n_{\text{pix}} = 1$, N_S is derived from the background number of photons (the background flux of the image), N_D is the total number of electrons caused by the dark current found from the dark image and N_R is the read out/shot noise of the pixel, calculated from the number of electrons. Note that each noise image has the same distortion correction and astrometry correction as the associated image frame (see Sections 3.7 and 3.10). Such analytic noise images are created for each associated image and used at the coadding stage.

3.10 Astrometry correction

The original archival pipeline performs an astrometry correction on a pointing, once it had been coadded, using the WCS. Due to the fact that most of the IRC frames have a positional offset, in turn due to incorrect telescope astrometry, which varies from frame to frame and can be as bad as 5 arcsec in the long wavelength channels. The optimized toolkit corrects for astronomical offsets on individual frames, before the coadding of them, since the offset can vary from frame to frame even within the same pointing. The jitter is believed to have been caused by changes in the temperature of the star trackers. The new archival pipeline makes an astrometry correction, if greater than five sources have been detected in a single frame. Sources can be difficult to detect in deep extragalactic images, and many are only detectable after coadding. In the archive processed data, these astrometry offsets have prevented successful processing of the faintest extragalactic deep fields (notably the ELAIS-N1 field discussed in Section 4.2). The archival pipeline coadds frames observed by the same filter in a single pointing and then corrects for any astrometric offset on the final coadded image. The optimized toolkit corrects for the astrometry offset on a frame-by-frame, filter-by-filter basis individually and independently of the other filters. The astrometry of the first frame in each pointing is corrected by aligning extracted point sources with the identical sources in the 2MASS or WISE galaxy catalogues, for NIR and

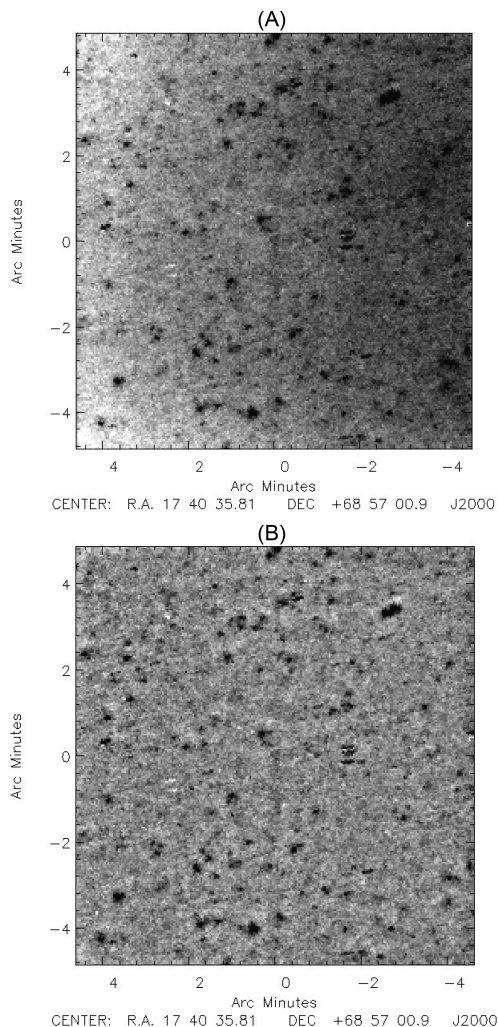


Figure 11. Image (a) shows the MIR-L detector affected by extended ghosting (light-scattered reflected off the array or filter, on to the detector). Image (b) shows the removal of the scattered light artefact by subtracting a boxcar median filtered image from the original frames (the coadded image is shown here for clarity).

MIR-S/MIR-L channels, respectively. Each subsequent frame of the same filter in the pointing is aligned to the first frame by matching the point sources. After the frames have been through the astrometry correction stage, they are ready to be coadded with frames from the same or other pointings.

3.11 Masking before coadding

Due to the increasing temperature of the telescope, as discussed in Section 3.5, and memory effects, images from the later stages of Phase 2 have artefacts that neither a dedicated flat-field nor hot pixel mask are able to remove. Two such artefacts are the ‘clover leaf’ pattern memory effect and vertical lines. These two artefacts can be seen in the coadded pointing in Fig. 12a. The ‘clover leaf’ memory effect is caused by imaging a very bright source in a previous pointing up to a few hours prior to the pointing in question. The artefact has the distinctive clover leaf pattern because the previous pointing observing the very bright source was dithered. The vertical lines are caused by a bright source observed on the IRC array during an AKARI/FIS scanning observation; hence, the artefact appears as

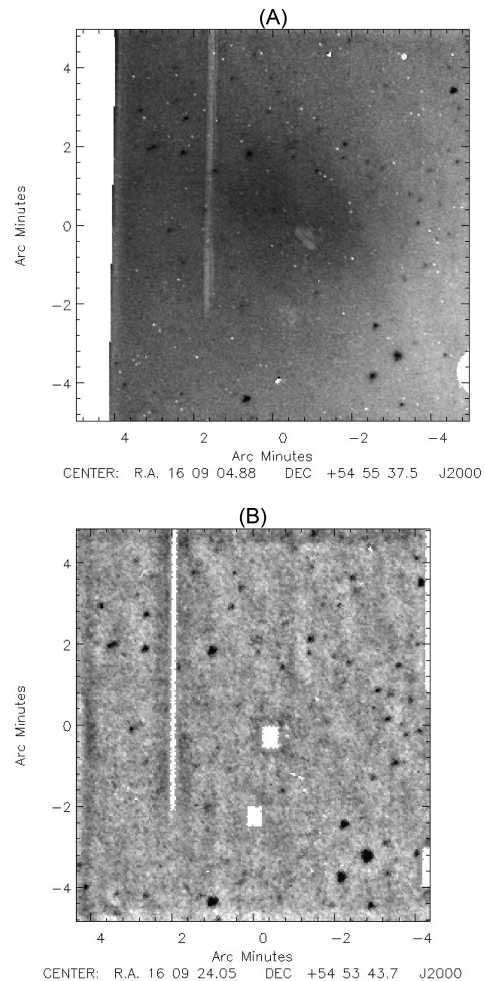


Figure 12. Example of masking frames before coadding. Image (a) shows a single pointing processed by the new archival pipeline (Egusa et al. 2016). Note the ‘clover leaf’ artefact in the centre of the image and just a little lower than centre and the vertical line. Image (b) shows the same pointing processed by the optimized toolkit. The vertical line and two ‘clover leaf’ memory effects have been masked in the individual frames before coadding. Also note the removal of the Earthshine light and masking of hot pixels. This image has been cropped, so as not to contain the slit area.

vertical lines. The same area is masked for all frames in a given pointing. Fig. 12 demonstrates the improvement to an extragalactic deep field by performing masking on individual frames.

Several ghost artefacts, found in AKARI images, have been discussed in previous work, e.g. Murata et al. (2013) discuss a ghost artefact created by a bright source reflected about the image pixel position coordinates $x = 115$, $y = 350$. An example of this artefact is shown in Fig. 13. This artefact was only present in the NIR images. The artefact was treated in a similar way to the memory effects discussed above, and masked where appropriate.

Arimatsu et al. (2011) discuss several ghost artefacts in the MIR bands, caused by bright sources. In the MIR-S channel, bright sources cause a ghost artefact, repeating at a period of about 24 pixels in the y-direction from the source. In both the MIR-S and MIR-L channels, bright sources produce a ghost artefact a little offset from the true source, and a set of two concentric artefacts, bigger than the original source. As the extragalactic fields discussed in this paper do not contain any overly bright sources in the MIR-S

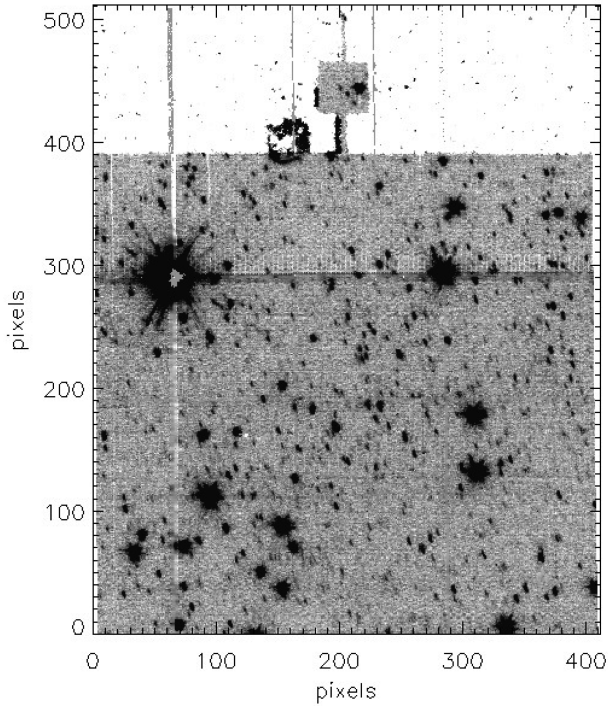


Figure 13. The figure shows one of the ghosts discussed in Murata et al. (2013). The ghost source can be seen at the bottom of the slit area, just left of centre. The source creating this ghost is the saturated source in the upper left of the image.

and MIR-L bands, it is observed that these artefacts are below the instrument noise level.

4 APPLICATION OF OPTIMIZED TOOLKIT

In order to quantify the improvement provided by the optimized toolkit compared to the archival data, the optimized toolkit was applied to three *AKARI* extragalactic survey fields. An example early- to mid-Phase 2 deep field was chosen, the IRAC Dark Field (Section 4.1) and an example late-Phase 2 deep field was also chosen, ELAIS North1 (hereafter ELAIS-N1, Section 4.2). The IRAC Dark Field, centred on $17^{\text{h}}40^{\text{m}}00^{\text{s}}$, $+69^{\circ}00'00''$ (J2000), was observed as an *AKARI* Open Time programme (PI: E. Egami) and is one of the deepest fields observed by *AKARI*. ELAIS-N1 was observed as part of the FU-HYU (Follow-Up Hayai-Yasui-Umai, PI: C. Pearson) *AKARI* Mission Programme (RA = $16^{\text{h}}09^{\text{m}}20^{\text{s}}$, Dec. = $+54^{\circ}57'00''$ J2000) (Pearson et al. 2010). An example shallow field, was also selected, the *AKARI* Deep Field South (PI: C. Pearson, proposal ID Open Time IRSEP, see Section 4.3) near the south ecliptic pole (hereafter SEP).

4.1 Case Study Deep-Field Early Phase 2: IRAC Dark Field

The IRAC Dark Field is a 20×20 arcmin area, in the north, centred on $17^{\text{h}}40^{\text{m}}00^{\text{s}}$, $+69^{\circ}00'00''$ (J2000), close to the NEP. This survey area was used in calibrating the instrumental background for *Spitzer*/IRAC, observed every 2–3 weeks over a 5+ week period (Krick et al. 2009). The IRAC Dark Field was also a calibration field for the SPIRE instrument on the *Herschel* Space Observatory and hence is one of the deepest extragalactic fields observed by *Herschel*. There is also a large amount of multiwavelength data for the IRAC Dark Field. With such a large amount of deep infrared data

Table 3. Observation log for the IRAC Dark Field pointings.

Pointing ID	Date	Filter	AOT
3030001-001	18/10/2006	N4 & S11	IRC05
3030001-003	18/10/2006	N4 & S11	IRC05
3030001-004	16/04/2007	N4 & S11	IRC05
3030001-005	19/10/2006	N4 & S11	IRC05
3030001-006	19/04/2007	N4 & S11	IRC05
3030001-007	27/10/2006	N4 & S11	IRC05
3030001-008	27/10/2006	N4 & S11	IRC05
3030001-009	27/10/2006	N4 & S11	IRC05
3030001-010	27/10/2006	N4 & S11	IRC05
3030001-011	28/10/2006	N4 & S11	IRC05
3030001-012	19/04/2007	N4 & S11	IRC05
3030001-013	20/04/2007	N4 & S11	IRC05
3030001-014	31/10/2006	N4 & S11	IRC05
3030001-015	21/04/2007	N4 & S11	IRC05
3030001-016	21/04/2007	N4 & S11	IRC05
3030001-017	21/04/2007	N4 & S11	IRC05
3030001-018	22/04/2007	N4 & S11	IRC05
3030001-019	22/04/2007	N4 & S11	IRC05
3030001-020	22/04/2007	N4 & S11	IRC05
3030002-001	10/10/2006	L15	IRC05
3030002-002	10/10/2006	L15	IRC05
3030002-003	12/10/2006	L15	IRC05
3030002-004	12/10/2006	L15	IRC05
3030002-005	23/04/2007	L15	IRC05
3030003-001	13/10/2006	L18W	IRC05
3030003-002	13/10/2006	L18W	IRC05
3030003-003	13/10/2006	L18W	IRC05
3030003-004	13/10/2006	L18W	IRC05
3030003-005	23/04/2007	L18W	IRC05
3031001-001	14/05/2007	L15	IRC05
3031001-002	14/05/2007	L15	IRC05
3031001-003	14/05/2007	L15	IRC05
3031001-004	15/05/2007	L15	IRC05
3031001-005	15/05/2007	L15	IRC05

from *Spitzer*, *AKARI* and *Herschel*/SPIRE, the IRAC Dark Field is a survey area of great importance. Data from all three telescopes have not as yet been fully utilized.

The IRAC Dark Field was chosen as a test of the optimized toolkit, as the observations are of a deep field observed during early to mid Phase 2. Though evident, the frames observed during this time period were not too badly affected by Earthshine light and hot pixels. One of the major issues for early-Phase 2 MIR-S frames is that they suffered from the so-called bean artefact, discussed in more detail in Section 3.4. Unlike the original and updated archival pipeline, the optimized toolkit is able to remove the bean artefact (see Fig. 4).

Table 3 shows the *AKARI*/IRC pointings of the IRAC Dark Field. There were 34 successful pointings of the IRAC Dark Field. It was observed 19 times by the N4 and S11 filters, 10 times by the L15 filter and 5 times by the L18W filter. Note half of the observations were observed 2006 October (late-Phase 1) and the other half were observed 2007 April/May (mid-Phase 2). The N4 and S11 frames were obtained during the same pointings. All pointings were observed using IRC05, the Astronomically Observed Template (AOT) for deep pointings. IRC05 was used, which does not have an option for dithered pointings. Due to the fact that each of these pointings covered roughly the same area of sky, this is one of the deepest fields observed by *AKARI*/IRC.

The individual frames were also checked for possible image ghosts discussed in Section 3.11, but none were found. Table 4

Table 4. IRAC Dark Field discarded frames.

Filter	Pointing ID	Frame number	Reason
S11	3030001_014	F004059008_S004	Artificial stripe pattern
L15	3031001_001	F008043439_L004	Cosmic ray
L15	3031001_004	F008048716_L002	Artificial stripe pattern
L15	3031001_004	F008048716_L003	Artificial stripe pattern
L15	3031001_004	F008048716_L004	Artificial stripe pattern
L15	3031001_004	F008048718_L002	Artificial stripe pattern
L15	3031001_004	F008048718_L003	Artificial stripe pattern
L15	3031001_004	F008048718_L004	Artificial stripe pattern

gives a list of damaged frames that were not used to create the IRAC Dark Field mosaicked images. In the table, the stripe artefact was caused by a cosmic ray, hitting the detector and saturating the entire node. This effect lasts for a few minutes, and can be seen in subsequent frames. Fig. 14 shows IRAC Dark Field final deep-field images from the optimized toolkit at 4.1, 11, 15 and 18 μm . The survey area of the IRAC Dark Field is 0.027 deg².

4.2 Case Study Deep-Field Late Phase 2: ELAIS-N1

The ELAIS-N1 was one of 11 fields making up the European Large Area ISO Survey (ELAIS Oliver et al. 2000, the largest open time survey performed by the Infrared Space Observatory, ISO Kessler et al. 1996). The ELAIS fields were selected at high Galactic latitudes (for ELAIS-N1 $\beta > 40^\circ$) for low cirrus emission ($I_{100\mu\text{m}} < 1.5 \text{ MJy sr}^{-1}$ cirrus level). ELAIS-N1 is one of the deepest surveys performed by *AKARI*. Out of all of the FU-HYU fields, it had the best visibility during the *AKARI* mission. ELAIS-N1 has a large amount of multiwavelength ancillary data (Cileigi et al. 1999; McMahon et al. 2001; Basilakos et al. 2002; Väisänen et al. 2002; Manners et al. 2003; Chary et al. 2004; Oliver et al. 2012).

ELAIS-N1 was chosen as a test of the optimized toolkit of a deep-field observed late-Phase 2; as apart from three of the pointings, which were observed mid-Phase 2, most of the observations (17 pointings) were made in late Phase 2. As discussed earlier in the paper, late-Phase 2 observations were plagued by many artefacts, e.g. Earthshine light, hot pixels, memory effects. Many of which

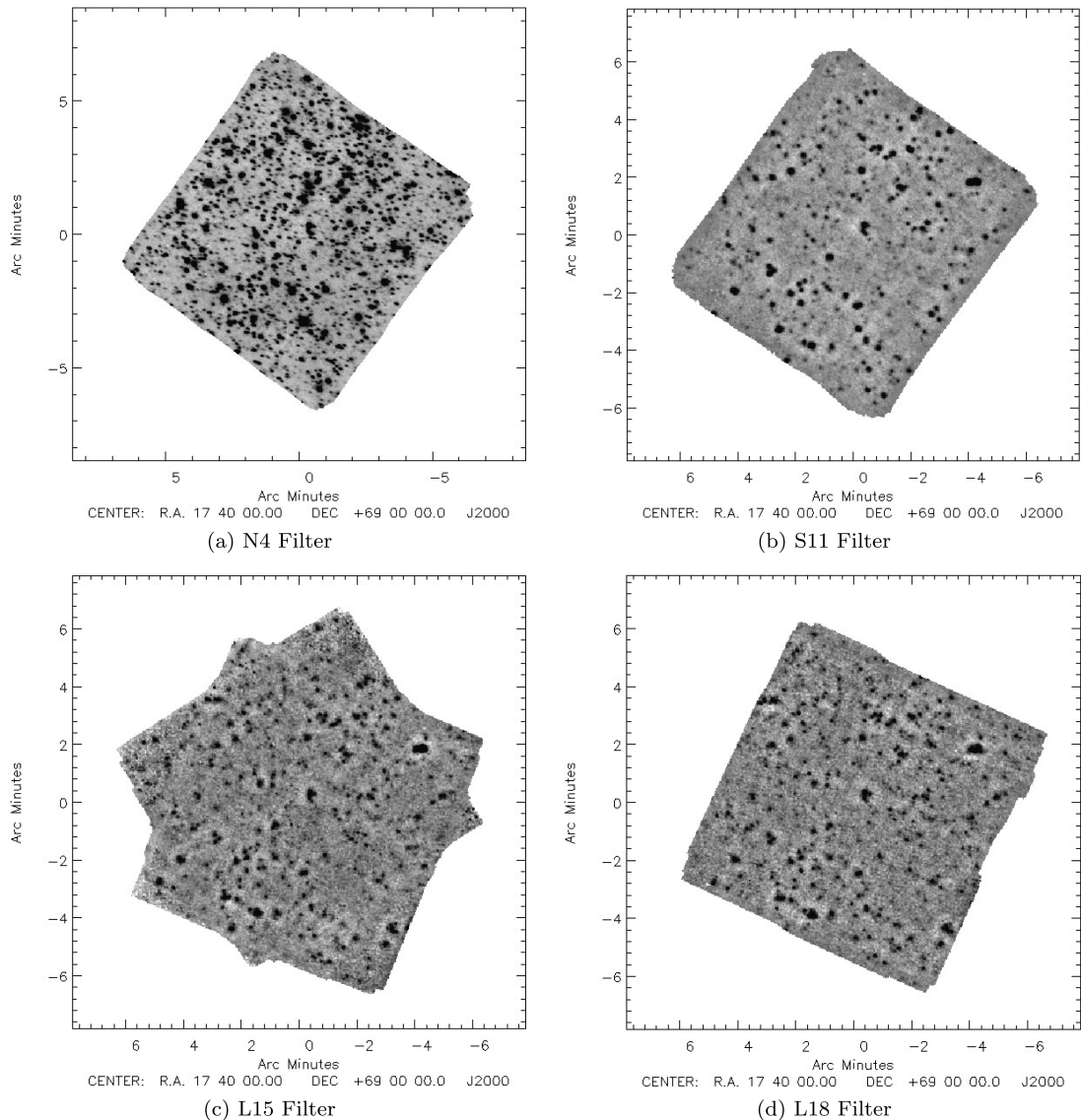
**Figure 14.** IRAC Dark Field mosaicked images.

Table 5. Observation log for the FU-HYU ELAIS-N1 pointings.

Pointing number	Date	Filter	AOT
1320226-001	19/07/2007	N4 & S11	IRC05
1320226-003	19/07/2007	N4 & S11	IRC05
1320226-004	19/07/2007	N4 & S11	IRC05
1320226-005	19/07/2007	N4 & S11	IRC05
1320226-006	20/07/2007	N4 & S11	IRC05
1320226-007	20/07/2007	N4 & S11	IRC05
1320235-001	21/07/2007	L15	IRC05
1320235-002	21/07/2007	L15	IRC05
1320235-003	21/07/2007	L15	IRC05
1320235-005	22/07/2007	L15	IRC05
1320013-001	16/01/2007	L15	IRC05
1320014-001	15/01/2007	L15	IRC05
1320015-001	17/01/2007	L15	IRC05
1320232-001	20/07/2007	L18W	IRC05
1320232-002	20/07/2007	L18W	IRC05
1320232-003	20/07/2007	L18W	IRC05
1320232-004	21/07/2007	L18W	IRC05
1320232-005	22/07/2007	L18W	IRC05
1320232-006	22/07/2007	L18W	IRC05
1320232-007	22/07/2007	L18W	IRC05

neither the original nor updated archival pipelines were able to fully remove.

Table 5 shows the observation log for the ELAIS-N1 pointings. All the pointings use astronomical template IRC05, which was not dithered. As the majority of the pointings are late Phase 2, they suffer from more Earthshine light than earlier observations. Section 3.8 shows how the most significant components of the Earthshine light were removed. The late-Phase 2 images also suffered from more detector deterioration. The time-dependent flat-field images and hot-pixel masks were created from independent observations taken over the same period as the ELAIS-N1 observations from 12/01/2007 to 21/01/2007 and 19/07/2007 to 22/07/2007. Due to the large areas of some pointings that required masking, the same area of each frame in a pointing was masked before coadding the pointing. Even though the ELAIS-N1 pointings were not dithered, since the frames are masked before coadding the intrinsic jitter of the telescope can be used effectively instead, to dither the observations to increase the total useable area of the frames.

Note that two of the ELAIS-N1 pointings, 1320235-002 and 1320235-003, taking in the IRC L15 band, had very significant offsets of up to 135 and 318 arcsec, respectively. It is thought that this was caused by the star tracker and telescope observing different parts of the sky (star tracker problem). Neither archival pipelines were able to coadd these two pointings; however, both of these large astronomical offsets were successfully corrected by the optimized toolkit (see Fig. 15).

The same as for the IRAC Dark Field frames, the images were checked for possible ghosts, but none were found. Although the optimized toolkit was successful in combining many frames, previously deemed unusable, there were a handful of incidences where frames still had to be discarded. Table 6 shows the frames, which were not used to create the new ELAIS-N1 deep-field image, with justification. Similar to the IRAC Dark Field frames, those with an artificial stripe pattern, caused by damage from a cosmic ray incident were removed. The single frame with many hot pixels was probably caused by protons or electrons trapped by the Earth's magnetic field hitting the detector. Fig. 16 shows the ELAIS-N1 final deep-field images from the optimized toolkit at 4.1, 11, 15 and 18 μm . The survey area of ELAIS-N1 is 0.028 deg^2 .

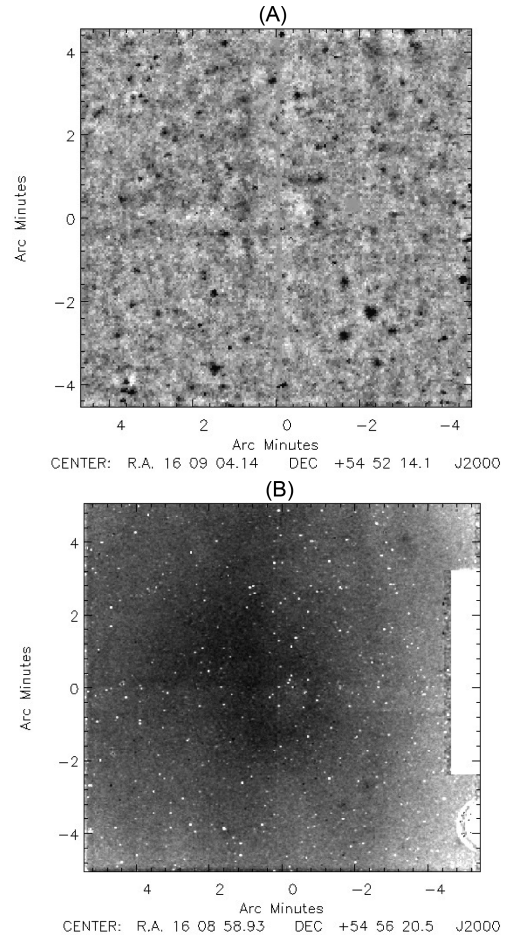


Figure 15. Example of the improvement provided by the optimized toolkit for the ELAIS-N1 L15 image 1320235-003 discussed in the text. Image (a) shows a single pointing processed by the optimized toolkit. This image has been cropped, so as not to contain the slit area. Image (b) shows the same pointing processed by the new archival pipeline (Egusa et al. 2016).

Table 6. ELAIS-N1 discarded frames.

Filter	Pointing number	Frame number	Reason
L18W	1320232_003	F009136797_L004	Artificial stripe pattern
L18W	1320232_003	F009136798_L002	Artificial stripe pattern
L18W	1320232_003	F009136798_L003	Artificial stripe pattern
L18W	1320232_003	F009136798_L004	Artificial stripe pattern
L18W	1320232_004	F009145059_L004	Many hot pixels

4.3 Case Study Shallow Field: ADF-S

The *AKARI* Deep Field South (hereafter ADF-S) is close to the SEP and was selected as the site for a large area survey (12 deg^2 centred on RA = 04^h44^m00^s, Dec. = −53°20′00″ J2000) at far-infrared wavelengths (Matsuura et al. 2011). In addition, the central 1 deg^2 area of the ADF-S was observed in *AKARI* Open Time, with the IRC (PI: C. Pearson). The ADF-S has also enjoyed extensive multi-wavelength follow-up observations (e.g. Scott et al. 2010; Valiante et al. 2010; Clements et al. 2011; Hatsukade et al. 2011; Oliver et al. 2012; White et al. 2012; Barrufet et al. in preparation).

ADF-S was chosen as a test of the optimized toolkit, as the IRC observations of the ADF-S form a shallow survey of overlapping single pointings. For the toolkit, the main difference with creating a mosaicked shallow field as apposed to a deep field is that shallow

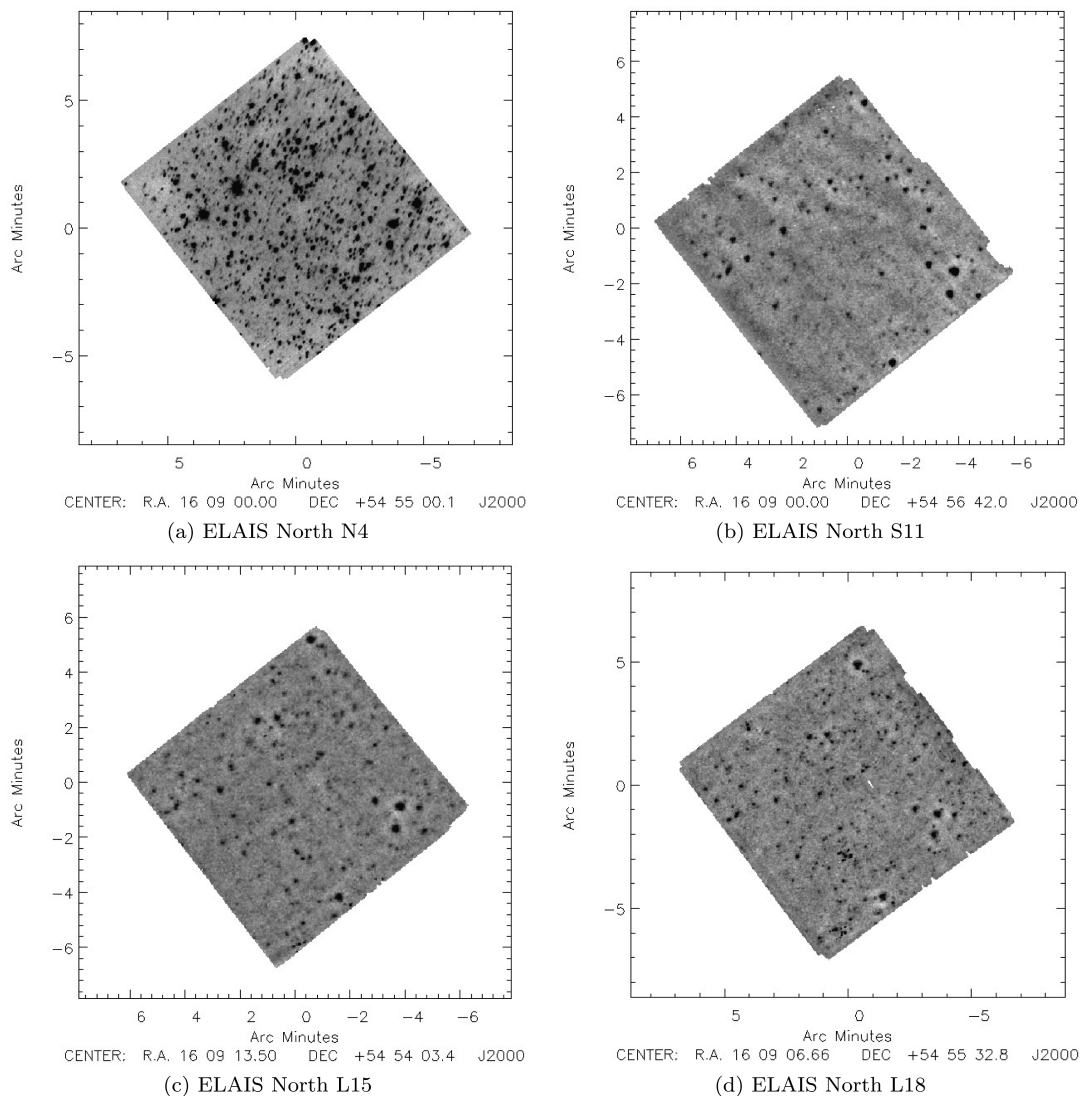


Figure 16. The ELAIS-N1 mosaicked images.

fields need careful removal of cosmic rays and hot pixels in the individual frames, due to the fact that not as many are removed in the coadding stage. Cosmic rays and hot pixels can be misidentified as point sources. For the case of the ADF-S, it is only three to four frames deep in the NIR images, compared to 30 frames deep in the case of ELAIS-N1. Unfortunately, this also means that many of the NIR frames required individual masking to remove an artefact only present in that frame, which is also visible in the coadded image. This also occurred in several of the MIR-S and L frames to a lesser extent. The NIR frames also require extra masking due to the *muxbleed* discussed in Section 3.2. Time-dependent flat-field images were created from an ensemble of independent *AKARI* observations over the same period as the ADF-S IRC observations (01-02-2007 to 09-02-2007). The ghosts and artefacts discussed in Section 3.11 are visible in one pointing (see Fig. 13) and have been masked.

Table 7 shows the observation log for the ADF-S pointings. All pointings were mid Phase 2 and used astronomical template IRC02. Table 8 shows the list of frames not used. In the table, ‘Flux Error’ refers to an effect only found on a final frame in a pointing and is caused by the shutter closing during integration. In addition, frames

that have high signal due to cosmic ray impact have also been removed. The effect of the cosmic ray lasts for a few minutes and can be seen in subsequent frames.

Fig. 17 shows the mosaicked ADF-S images in the six *AKARI*/IRC filters at 3.2, 4.1, 7, 11, 15 and 24 μm . As the L24 filter was the least sensitive of the *AKARI*/IRC filters and the ADF-S is a shallow field, *SEXTRACTOR* was unable to detect a statistically meaningful number of sources, i.e. only 14 sources. It was decided that further analysis of the ADF-S L24 image with a different source extraction method would not be beneficial, as there already exists a large amount of deep *Spitzer*/MIPS 24 μm data over the same field area from Clements et al. (2011). The survey area of the ADF-S is 0.46 deg^2 .

5 RESULTS

5.1 Source extraction and photometry

Source extraction was made using *SEXTRACTOR* (Bertin & Arnouts 1996) on the mosaicked images to create the source catalogues for the IRAC Dark Field, ELAIS-N1 and ADF-S fields. The

Table 7. Observation log for ADF-S.

Pointing number	Date	Filter	AOT
320001-001	03/02/2007	N3 N4 S7 S11 L15 L24	IRC02
320002-001	04/02/2007	N3 N4 S7 S11 L15 L24	IRC02
320003-001	04/02/2007	N3 N4 S7 S11 L15 L24	IRC02
320004-001	05/02/2007	N3 N4 S7 S11 L15 L24	IRC02
320005-001	03/02/2007	N3 N4 S7 S11 L15 L24	IRC02
320006-001	04/02/2007	N3 N4 S7 S11 L15 L24	IRC02
320007-001	05/02/2007	N3 N4 S7 S11 L15 L24	IRC02
320008-001	06/02/2007	N3 N4 S7 S11 L15 L24	IRC02
320009-001	03/02/2007	N3 N4 S7 S11 L15 L24	IRC02
320010-001	05/02/2007	N3 N4 S7 S11 L15 L24	IRC02
320011-001	05/02/2007	N3 N4 S7 S11 L15 L24	IRC02
320012-001	06/02/2007	N3 N4 S7 S11 L15 L24	IRC02
320013-001	09/02/2007	N3 N4 S7 S11 L15 L24	IRC02
320014-001	08/02/2007	N3 N4 S7 S11 L15 L24	IRC02
320015-001	07/02/2007	N3 N4 S7 S11 L15 L24	IRC02
320016-001	07/02/2007	N3 N4 S7 S11 L15 L24	IRC02
320017-001	09/02/2007	N3 N4 S7 S11 L15 L24	IRC02
320018-001	08/02/2007	N3 N4 S7 S11 L15 L24	IRC02
320019-001	07/02/2007	N3 N4 S7 S11 L15 L24	IRC02
320021-001	09/02/2007	N3 N4 S7 S11 L15 L24	IRC02
320042-001	07/02/2007	N3 N4 S7 S11 L15 L24	IRC02
320046-001	08/02/2007	N3 N4 S7 S11 L15 L24	IRC02
320050-001	05/02/2007	N3 N4 S7 S11 L15 L24	IRC02

Table 8. ADF-S discarded frames.

Filter	Pointing number	Frame number	Reason
N4	3200002_001	F006033902_N002	Many hot pixels
S7	3200004_001	F006038908_S004	Flux error
L15	3200003_001	F006036697_L003	Cosmic ray
L15	3200003_001	F006036697_L004	Cosmic ray
L15	3200004_001	F006038908_L004	Flux error
L24	3200003_001	F006036693_L004	Many hot pixels
L24	3200003_001	F006036699_L002	Cosmic ray
L24	3200003_001	F006036699_L003	Cosmic ray
L24	3200003_001	F006036699_L004	Cosmic ray
L24	3200006_001	F006034162_L002	Artificial stripe pattern
L24	3200006_001	F006034162_L003	Artificial stripe pattern
L24	3200006_001	F006034162_L004	Artificial stripe pattern

parameters for SExtractor were based on those used in Murata et al. (2013) for the *AKARI* North Ecliptic Pole (NEP) survey. The main differences compared to those used on the NEP field were for the NIR and MIR-L channel images, where the SExtractor parameters DETECT_MINAREA and DETECT_THRESH were set to 5 pixels and 3σ , respectively, and for the MIR-S channel image where they were set to 5 pixels and 3.5σ , respectively. These settings were optimized to have the lowest number of false source detections (see Section 5.2), while maintaining the highest number of true source detections. SExtractor aperture photometry was used to measure the extracted source flux, using the flux conversion from ADUs to Janskys from Tanabé et al. (2008) and aperture corrections from Arimatsu et al. (2011), both listed in Table 9.

5.2 Reliability

To test the reliability of the source extraction, a negative image was created for each mosaicked image during the coadding stage. SExtractor was then applied to this negative image using the same settings. Table 10 shows the percentage of sources detected in the

negative image to the source detections in the original image in order to provide a measure of the possible number of false detections. Reliability corrections were performed as a function of source flux, where the number of extracted negative sources was greater than 1 per cent. The large number of spurious sources in all of the IRAC Dark Field S11 and ELAIS-N1 MIR images is attributed to Earthshine light not having been fully removed.

5.3 Completeness

To correct for sources missed by the source extraction process (completeness), Monte Carlo simulations were used to inject artificial sources of known location and flux into each mosaicked image. After a single artificial source had been injected into an image, the image was run through SExtractor. This was repeated 1000 times for each flux bin for the deep IRAC Dark Field and ELAIS-N1 field in each channel. After performing an initial test of completeness, it was found that the NIR band ADF-S images required much less of a completeness correction than the other bands and fields. It was decided 1000 simulations were not required for the ADF-S N3 and N4 images, whereas it was necessary for the other images. Therefore, the ADF-S NIR band images each had 100 simulations and the ADF-S MIR-S and L-band images had 1000 simulations. Figs 18–20 show the completeness curves (the ratio of successfully extracted sources to total number of sources) as a function of input source flux for the IRAC Dark Field, ELAIS-N1 and ADF-S source counts.

The completeness for the deep IRAC Dark Field drops off steeply with the 50 per cent completeness levels in the N4, S11, L15 and L18W bands being 0.008, 0.04, 0.105 and 0.107 mJy respectively. Whereas the completeness for the deep ELAIS-N1 field drops off gradually with the 50 per cent completeness levels in the N4, S11, L15 and L18W bands being 0.009, 0.06, 0.12 and 0.10 mJy, respectively. There is not obvious reason for the broad shoulder at around 80 per cent in the completeness curve for the L15 band in ELAIS-N1 field, and there are likely to be several factors causing this. One possible reason could be that the final image has higher background noise levels than the other images, which could be due to a combination of the filter and detector deterioration (late-Phase 2), or caused by too much smoothing to remove the Earthshine light artefact. Another reason could be related to the small-scale noise caused by the confusion in the field, or there may be some structure along the line of sight by chance. The completeness correction for the shallower ADF-S field shows a very steep turnover in all bands at around the 90 per cent level, with corresponding 50 per cent completeness levels in the N3, N4, S7, S11 and L15 bands of 0.07, 0.04, 0.18, 0.20 and 0.35 mJy, respectively.

5.4 Stellar subtraction

Especially in the shorter wavebands of the IRC, the contribution to the source counts from stars can be significant and must be removed. Stellar subtraction was performed using catalogues at optical wavelengths to identify stars in the *AKARI* fields. Stars in the IRAC Dark Field and ELAIS-N1 images were identified using the Automatic Plate Measuring (APM) machine data from the Palomar Observatory Sky Survey 1 (Maddox et al. 1990). *AKARI* sources was crossed matched with the APM star positions, with a search radius of 4 arcsec. This search radius was chosen as it was representative of the sources' PSF. Matched sources were removed from the source catalogues. On the rare occasion that there were two or more extracted sources within the radius, the extracted source

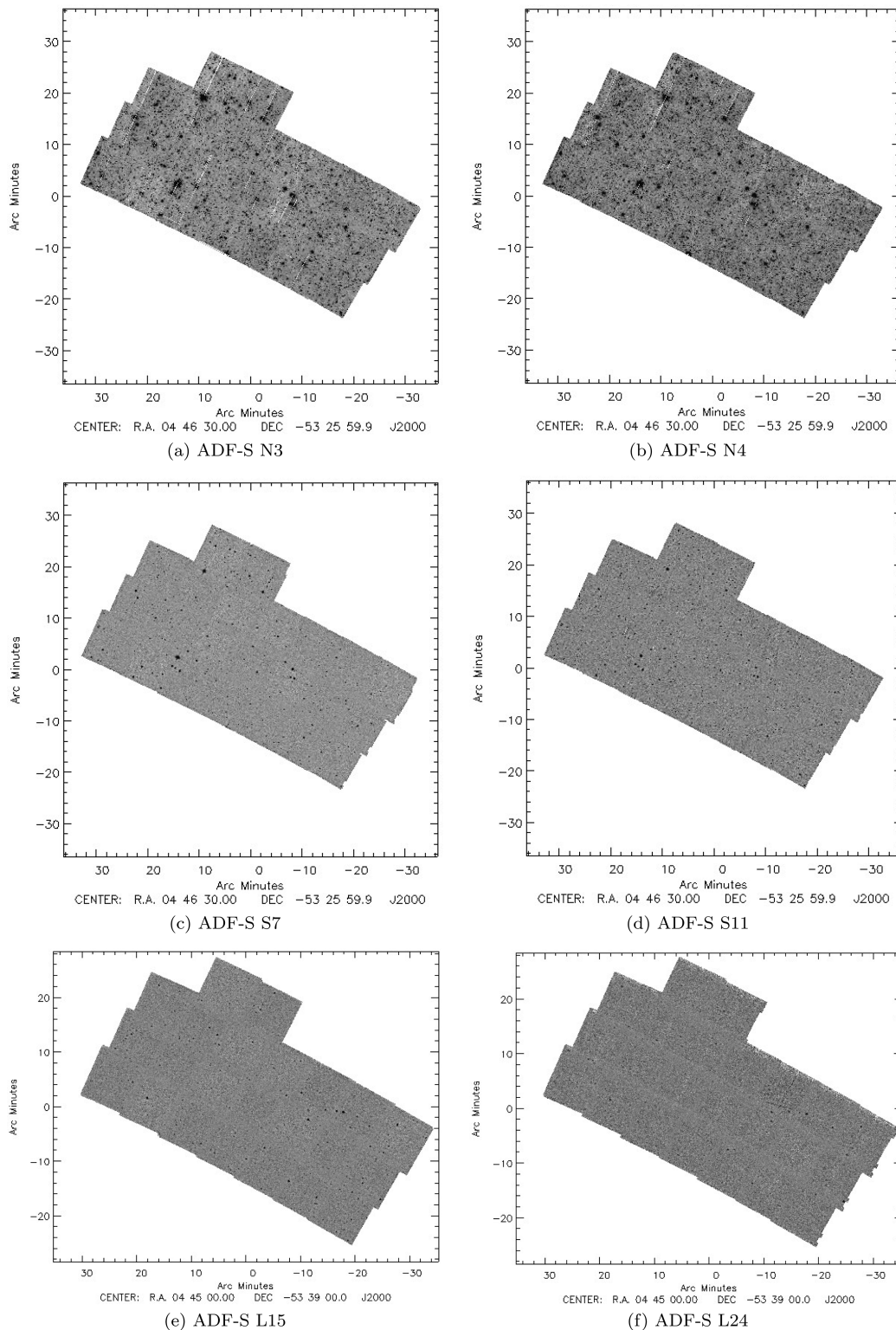


Figure 17. The ADF-S mosaicked images.

closest to the APM location was removed. Tables 11 and 12 show the IRAC Dark Field and ELAIS-N1 stellar fraction, respectively, as a function of flux density. For the ADF-S, the star positions were found using the *R*-band MOSAIC (CITO) data (Barrufet et al. in

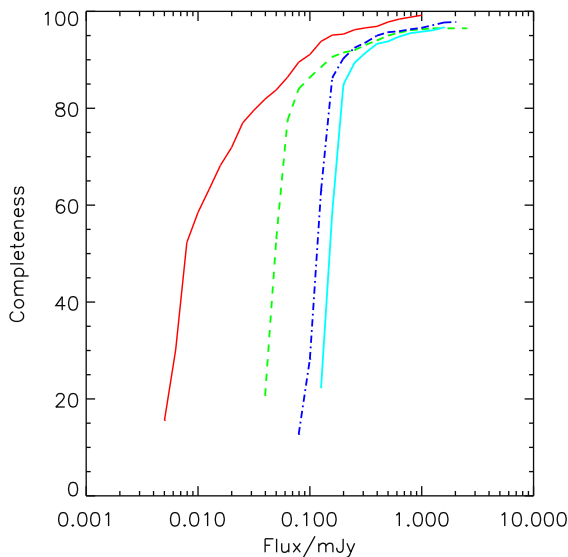
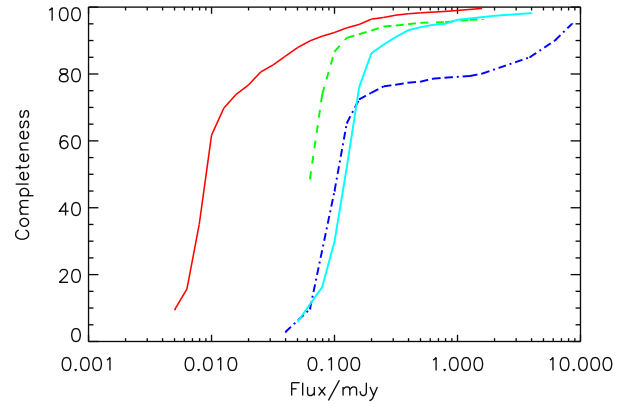
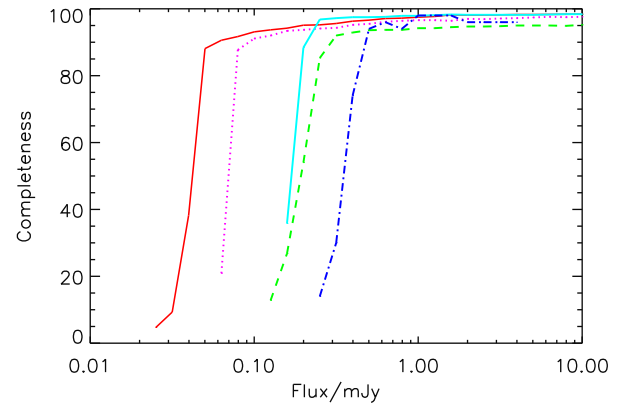
preparation), where coverage was available. The stellar fraction for each filter was then calculated assuming the same fraction over the entire ADF-S area. Table 13 shows the ADF-S stellar fraction as a function of flux density.

Table 9. Table showing the flux conversion and aperture corrections for the filters used in the IRAC Dark Field, ELAIS-N1 and ADF-S fields.

Filter	Flux conversion N_{ADU} to Jy	Aperture correction
N3	0.4394×10^{-6}	0.873
N4 IRC03	0.2584×10^{-6}	0.871
N4 IRC05	0.1753×10^{-6}	0.871
S7	1.0220×10^{-6}	0.918
S11	0.7732×10^{-6}	0.902
L15	1.6910×10^{-6}	0.852
L18W	1.1460×10^{-6}	0.793
L24	4.8920×10^{-6}	0.685

Table 10. Table showing the percentage of sources extracted from the negative image compared to the total number of sources in the original image, as a measure of the reliability of the source extraction.

Field	Filter	Negative sources (%)
IRAC Dark Field	N4	0.21
	S11	5.05
	L15	2.67
	L18W	0
ELAIS-N1	N4	0
	S11	9.48
	L15	2.42
	L18W	6.15
ADF-S	N3	0.03
	N4	0.06
	S7	0
	S11	3.57
	L15	0
	L24	0

**Figure 18.** The completeness curves for IRAC Dark Field. The completeness for N4 is the red solid line, the completeness for S11 is the green dashed line, the completeness for L15 is the blue dot-dashed line, and the completeness for L18W is the cyan dot-dot-dot-dashed line.**Figure 19.** The completeness correction curve for ELAIS-N1. The completeness for N4 is the red solid line, the completeness for S11 is the green dashed line, the completeness for L15 is the blue dot-dashed line, and the completeness for L18W is the cyan dot-dot-dot-dashed line.**Figure 20.** The completeness correction curve for ADF-S. The completeness for N3 is the magenta dotted line, the completeness for N4 is the red solid line, the completeness for S7 is the cyan dot-dot-dot-dashed line, the completeness for S11 is the green dashed line and the completeness for L15 is the blue dot-dashed line.

5.5 Galaxy source counts and catalogues

The final normalized differential source counts per steradian as a function of flux density (S) as $(dN/dS)S^{2.5}$ are plotted in Figs 21, 22 and 23 for the IRAC Dark Field, ELAIS-N1 and ADF-S fields, respectively. The counts have been corrected for completeness, reliability and stellar contributions. The source counts for each band are also tabulated in Tables 14–17 for IRAC Dark Field, Tables 18–21 for ELAIS-N1 and Tables 22–26 for the ADF-S field.

The uncertainty in the source counts, $\sigma(N)$, was calculated using equation (4):

$$\sigma(N) = \sqrt{N_{\text{obs}}} \left[\left(\frac{1}{f_{\text{com}}} \right)^2 + N_{\text{obs}} \left(\left(\Delta f_{\text{com}} \frac{1}{f_{\text{com}}^2} \right)^2 \right) \right]^{\frac{1}{2}} \times \frac{S^{2.5}}{\Delta S \times A}, \quad (4)$$

where N_{obs} is the number of galaxies in a given flux bin centred on flux S , f_{com} is the completeness fraction and A is the area of the survey. For the work of the paper Δf_{com} (the standard deviation of f_{com}) is given by $\frac{\sqrt{f_{\text{com}}(1-f_{\text{com}})}}{T}$, where T is the total number of injected sources for the flux bin in question. The reliability is assumed to

Table 11. Stellar contribution to the source counts as a function of flux density for the IRAC Dark Field.

Flux (/mJy)	N4 (%)	S11 (%)	L15 (%)	L18W (%)
0.008	0.0	–	–	–
0.010	1.35	–	–	–
0.013	0.0	–	–	–
0.016	2.86	–	–	–
0.020	1.28	–	–	–
0.025	1.30	0.00	–	–
0.032	1.72	0.00	–	–
0.040	3.28	3.33	–	–
0.050	4.17	17.39	–	–
0.063	3.03	12.90	–	0.00
0.079	15.63	9.09	0.0	0.00
0.100	7.14	25.00	0.0	0.00
0.126	27.78	0.0	3.03	0.00
0.158	30.77	18.75	0.0	4.00
0.200	16.67	25.00	6.67	0.00
0.251	50.00	8.33	3.03	3.13
0.316	55.56	14.29	5.56	0.00
0.398	80.00	20.00	0.00	0.00
0.501	66.67	20.00	0.00	16.67
0.631	66.67	25.00	0.00	0.00
0.794	100.00	0.00	0.0	0.00
1.000	50.00	0.00	0.00	0.00
1.259	–	0.00	–	–
1.585	100.00	–	0.00	0.00

Table 12. Stellar contribution to the source counts as a function of flux density for the ELAIS-N1 field.

Flux (/mJy)	N4 (%)	S11 (%)	L15 (%)	L18W (%)
0.008	0.0	–	–	–
0.010	0.0	–	–	–
0.013	0.0	–	–	–
0.016	1.32	–	–	–
0.020	0.0	–	–	–
0.025	2.60	–	–	–
0.032	3.45	–	–	–
0.040	3.33	–	0.0	–
0.050	8.00	–	–	0.0
0.063	7.69	00	0.0	–
0.079	6.25	11.37	–	0.0
0.100	14.29	24.36	0.0	0.0
0.126	13.64	4.89	0.0	0.0
0.158	11.11	7.99	0.0	0.0
0.200	46.15	0.0	4.93	0.0
0.251	42.86	6.64	0.0	12.50
0.316	71.43	19.57	0.0	0.0
0.398	75.00	0.0	0.0	0.0
0.501	80.00	0.0	33.333	–
0.631	83.33	31.72	0.0	–
0.794	0.0	0.0	0.0	0.0
1.000	0.0	–	–	0.0
1.259	–	0.0	0.0	0.0
1.585	–	0.0	0.0	–
1.995	0.0	–	0.0	–
3.981	100.00	–	–	0.0

Table 13. Stellar contribution to the source counts as a function of flux density for the ADF-S field.

Flux (/mJy)	N3 (%)	N4 (%)	S7 (%)	S11 (%)	L15 (%)
0.025	–	0.0	–	–	–
0.032	–	0.0	–	–	–
0.040	–	0.0	–	–	–
0.050	–	0.0	–	–	–
0.063	0.0	0.0	–	–	–
0.080	0.0	0.25	–	–	–
0.100	0.0	3.10	–	–	–
0.126	0.0	5.30	–	0.0	–
0.158	0.33	7.81	0.0	0.0	–
0.200	1.30	22.82	29.91	8.44	–
0.251	4.02	18.76	21.19	8.44	0.0
0.316	13.07	38.99	18.31	10.39	0.0
0.398	19.50	41.42	31.22	11.33	0.0
0.501	18.80	71.20	41.74	11.00	3.85
0.631	37.21	68.42	53.63	11.52	12.16
0.794	49.37	84.21	65.28	14.44	18.37
1.000	59.48	84.21	61.74	15.31	12.90
1.259	76.91	90.95	81.35	22.03	18.18
1.585	80.07	90.23	74.51	34.23	53.85
1.995	86.16	63.16	48.42	50.66	50.00
2.512	88.77	92.63	86.44	37.25	50.00
3.162	96.09	89.16	90.79	29.80	50.00
3.981	81.46	–	81.72	75.99	33.33
5.012	75.20	84.21	98.87	70.37	100.00
6.310	100.00	78.95	80.89	46.06	100.00
7.943	95.84	100.00	84.74	50.66	100.00
10.000	83.55	100.00	95.34	54.28	100.00
12.589	100.00	63.16	76.27	100.00	100.00
15.849	96.41	63.16	42.37	100.00	100.00
19.953	83.55	–	95.33	0.0	–
25.119	62.66	100.00	84.74	100.00	100.00
31.623	62.66	–	100.00	100.00	–
39.811	100.00	–	–	–	–
63.096	–	–	100.00	–	–
158.489	–	–	100.00	–	–

be negligible, and thus, an uncertainty term for reliability is not included in the equation. When calculating the uncertainty for the case of small number statistics of a single galaxy in a flux bin, the Poisson term is replaced by $1^{+0.95}_{-0.827}$ (Gehrels 1986).

The *AKARI*/IRC galaxy catalogues of the IRAC Dark Field, ELAIS-N1 and ADF-S are available for public download. Table 27 gives an example of the IRAC Dark Field galaxy catalogue.

6 COMPARISON WITH OTHER SURVEYS AND MODELS

The source counts derived from the optimized toolkit are compared in Fig. 24 with previously published work from Murata et al. (2014a) who presented *AKARI* source counts from the NEP field, a $\sim 0.5 \text{ deg}^2$ area, using all nine photometric bands of the IRC, located at (RA = $17^{\text{h}}56^{\text{m}}$, Dec. = $66^{\circ}37'$) just offset from the ecliptic pole. Also shown are the *Spitzer* galaxy counts where available, from Fazio et al. (2004), and the $16 \mu\text{m}$ counts from Teplitz et al. (2011) from the *Spitzer* InfraRed Spectrograph (IRS) peak-up camera.

To interpret the results, the source counts are compared to two different galaxy evolution models. The Pearson phenomenological backwards evolution model (Pearson 2005; Pearson & Khan 2009) has provided a good fit to source counts from the near-infrared to

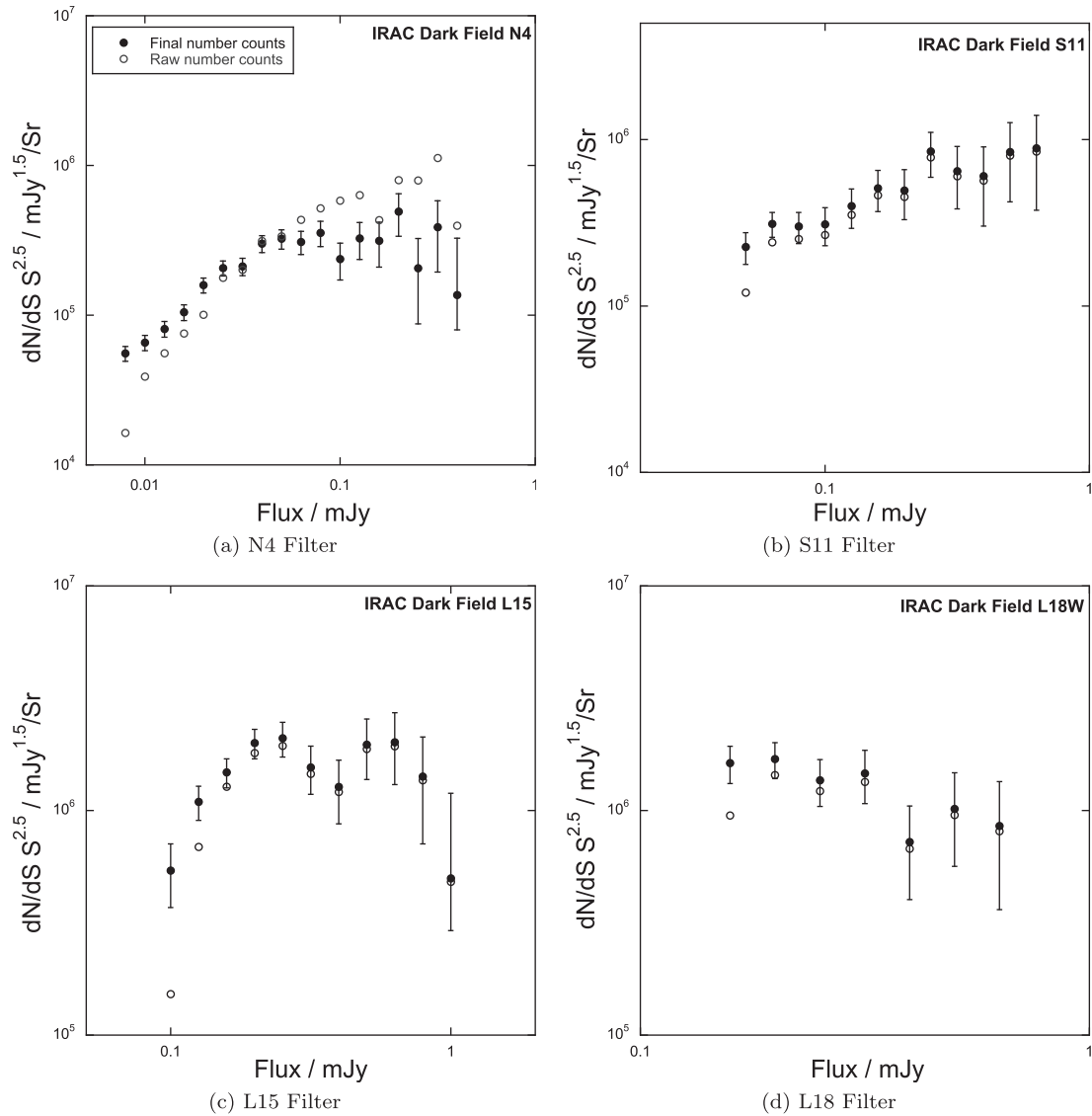


Figure 21. IRAC Dark Field Euclidean source counts per unit area. The open circles are the raw source counts, and the filled circles give the completeness and reliability-corrected, stellar-subtracted galaxy source counts. Note for image clarity, only the final source counts have their associated errors in the graphs.

millimetre wavelengths. The Pearson model is made up of six different population types: normal quiescent, elliptical, star-forming, luminous infrared galaxies (LIRGs), ultra luminous infrared galaxies (ULIRGs) and AGN. The model evolves the separate galaxy populations in luminosity ($F(z)$) and density ($G(z)$), both as a function of redshift. The parametrization for both the evolution in luminosity and density are described as a double power law up to $z \sim 2$. The power laws are dependent on galaxy type. At $z > 2$, both the luminosity and density evolution decline to higher redshifts. The Pearson galaxy evolution model has strong links with *AKARI*, as it was influential in deciding the wavelength of the near and mid-infrared filters.

The galaxy evolution model of Cai et al. (2013), also known as and hereafter referred to as the SISSA model) is a hybrid model using a combination of physical and phenomenological models. The galaxy populations have been divided into high- z ($z \geq 1.5$), proto-spheriods and AGN, and low- z ($z < 1.5$), late-type ‘cold’ galaxies and ‘warm’ starburst galaxies. To model the high- z population, Cai et al. (2013) use a bolometric luminosity function for spheroidal galaxies and

SEDs for the high- z AGN; these are used in a physical forward evolution model, based on Granato et al. (2004). To model the low- z populations, Cai et al. (2013) use a parametric phenomenological backward evolution model. The low- z population is subdivided into ‘warm’ starburst galaxies, ‘cold’ late-type galaxies, type-1 AGN and type-2 AGN, where the AGN have been ‘reactivated’. Using their galaxy evolution models, Cai et al. (2013) have created luminosity functions, SEDs and source count.

Both the Pearson and the SISSA models are plotted with the observed source counts in Fig. 24.

The source counts at $3.2 \mu\text{m}$ are shown in Fig. 24a. The source counts from this work lie slightly above the *AKARI* NEP counts of Murata et al. (2014a) but are consistent within the errors. However, there appears to be a significant offset when compared with the IRAC counts of (Fazio et al. 2004), although the scatter is large. Some of this difference may be due to stellar subtraction. Note that the optical data used for stellar subtraction did not provide full coverage of the area; therefore, the fractional stellar contribution was derived statistically. As there are very few stars in the observed

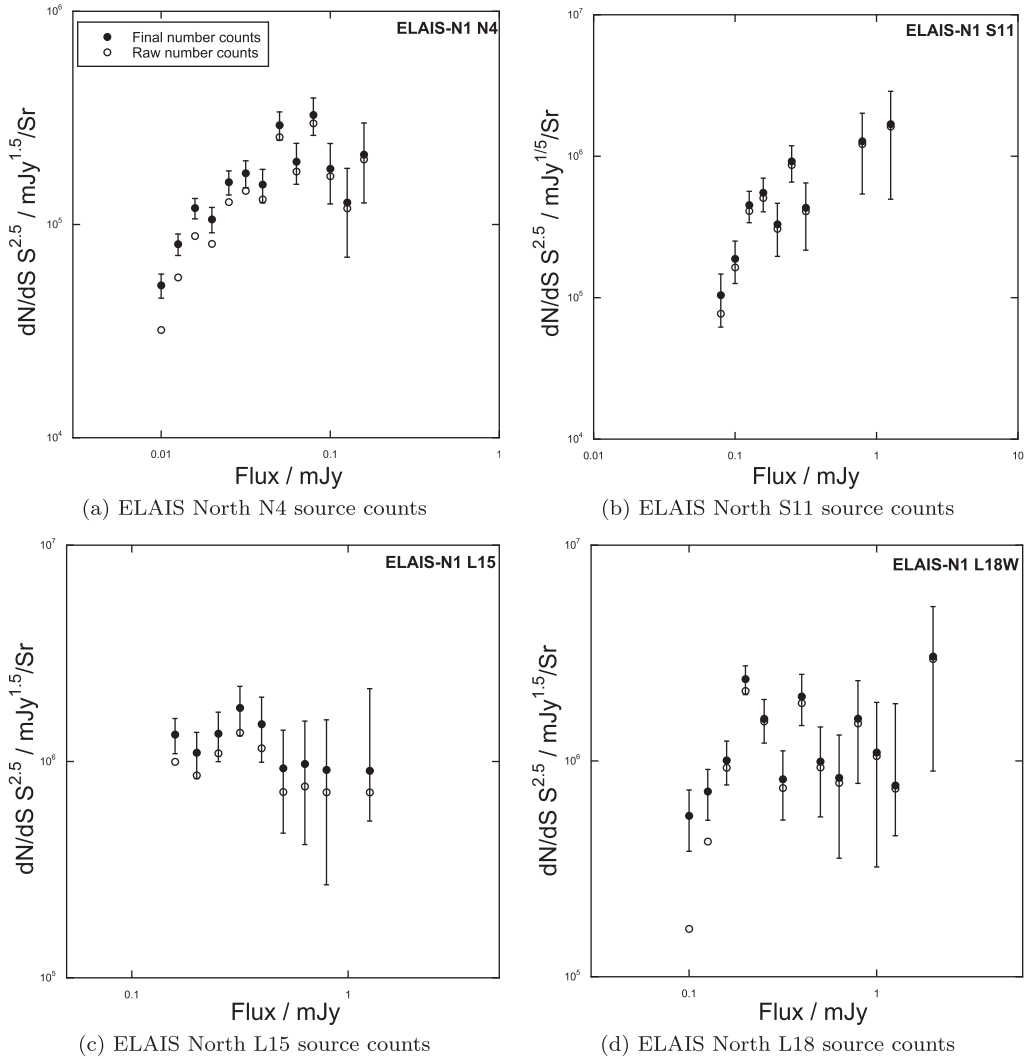


Figure 22. The ELAIS-N1 source counts. The open circles give the raw counts, and the filled circles give the completeness and reliability-corrected, stellar-subtracted galaxy source counts. Note for image clarity, only the final source counts have their associated errors in the graphs.

area, the scaling is likely to be affected by small number statistics. In this band, the Pearson model is in better agreement with the IRAC 3.6 μm counts. The counts of Murata et al. (2014a) exhibit a faint upturn at the faintest fluxes not seen in the ELAIS-N1 number counts or predicted by the model.

The source counts at 4.1 μm are shown in Fig. 24b for both the IRAC Dark Field, ELAIS-N1 and ADF-S fields. The counts are compared with the *AKARI* NEP, the IRAC 4.5 μm counts and the Pearson evolutionary model. The observed counts span a large range in flux density from ~ 2 to 0.01 mJy with the wider ADF-S field constraining the bright end of the source counts ($S > 2$ mJy) and the fainter counts covered by the deeper IRAC Dark Field and ELAIS-N1 field. The source counts derived from the optimized toolkit are in good agreement with the IRAC 4.5 μm counts at all flux densities. The faint end slope of the source counts appears steeper for the counts presented here compared with the IRAC counts, and the Pearson model predicts an even shallower slope to the faint end of the source counts. At this faint level, the counts are probing the region between the dust emission and stellar contribution within galaxies, where the assumed spectral energy distribution (SED) for the models are not well constrained.

Fig. 24c shows the *AKARI* 7 μm counts in the ADF-S (neither the IRAC Dark Field nor ELAIS-N1 were observed in this band) plotted together with the *AKARI* NEP and the IRAC 8 μm counts. The ADF-S counts are in good agreement with the IRAC 8 μm over the $0.2 < S < 10$ mJy flux range. The SISSA models appear to fit the ADF-S counts better than the Pearson model. However, the Pearson model and *AKARI* NEP counts are in agreement, although the errors on the NEP counts are very large. It should be noted that even at this longer wavelength, the reliability of the stellar subtraction method can affect the source counts at the brightest flux levels.

The 11 μm source counts are shown in Fig. 24d for both the IRAC Dark Field, ELAIS-N1 and ADF-S fields compared with the *AKARI* NEP counts and the Pearson and SISSA models. The 11- μm band was unique to *AKARI* and there are no *Spitzer* counts in this waveband. The IRAC Dark Field and the NEP counts appear to be in agreement. There is a significant scatter in the ELAIS-N1 counts possibly due to remnants of Earthshine, since out of the four filters observed in the ELAIS-N1 field, the S11 band had the worst Earthshine effect. In this band, the observations cannot distinguish between the models (which are themselves quite similar), but the Pearson model appears to fit the IRAC Dark Field better at fainter

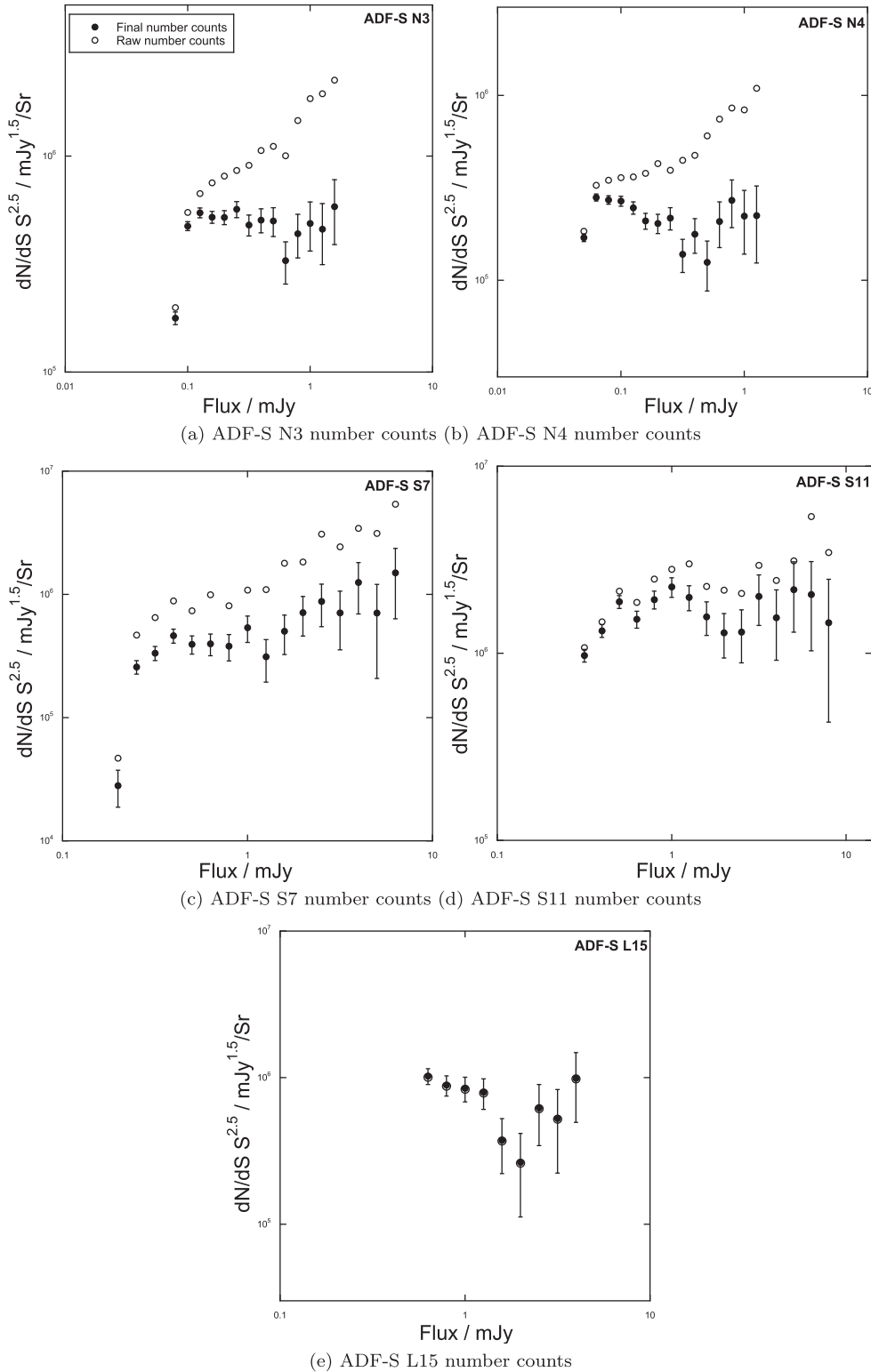


Figure 23. The ADF-S number counts. The open circles give the raw counts, and the filled circles give the completeness and reliability-corrected, stellar-subtracted galaxy source counts. Note the L15 raw and final source counts are very similar. Also note for image clarity, only the final source counts have their associated errors in the graphs.

fluxes, whereas the SISSA model appears to fit the brighter counts better. Fig. 24d shows that the S11 number counts are deeper than those of Murata et al. (2014a), the previous deepest 11 μ m counts. Thus, the *AKARI*/IRAC Dark Field 11 μ m image created in this

paper, shown in Fig. 14b, is currently the deepest 11 μ m image of the sky.

Fig. 24e shows the source counts at 15 μ m for the IRAC Dark Field, ELAIS-N1 and the ADF-S fields. Also plotted are the *AKARI*

Table 14. Final normalized differential source counts, $dN/dSS^{2.5}$, presented logarithmically as $mJy^{1.5} sr^{-1}$ for the N4 band in the IRAC Dark Field, with associated errors also presented logarithmically, reliability and completeness.

Log ₁₀ flux (/mJy)	Flux (/mJy)	Log ₁₀ final (Counts)	Log ₁₀ (Error)	Rel (%)	Com (%)
-2.10	0.008	4.74	0.05	100.0	52.3
-2.00	0.010	4.82	0.05	100.0	58.5
-1.90	0.013	4.91	0.05	100.0	63.3
-1.80	0.016	5.02	0.05	100.0	68.2
-1.70	0.020	5.20	0.05	100.0	71.9
-1.60	0.025	5.32	0.05	100.0	77.0
-1.50	0.032	5.37	0.06	100.0	79.6
-1.40	0.040	5.48	0.06	100.0	81.9
-1.30	0.050	5.51	0.06	100.0	83.8
-1.20	0.063	5.49	0.08	100.0	86.4
-1.10	0.079	5.55	0.08	100.0	89.5
-1.00	0.100	5.38	0.12	100.0	91.1
-0.90	0.126	5.51	0.12	100.0	93.8
-0.80	0.158	5.50	0.14	100.0	95.1
-0.70	0.200	5.69	0.14	100.0	95.3
-0.60	0.251	5.32	0.25	100.0	96.2
-0.50	0.316	5.59	0.22	100.0	96.6
-0.40	0.398	5.13	0.18	100.0	96.9
-0.30	0.501	5.28	0.18	100.0	97.8
-0.20	0.631	5.43	0.18	100.0	98.4

Table 15. Final normalized differential source counts, $dN/dSS^{2.5}$, presented logarithmically as $mJy^{1.5} sr^{-1}$ for the S11 band in the IRAC Dark Field, with associated errors also presented logarithmically, reliability and completeness.

Log ₁₀ flux (/mJy)	Flux (/mJy)	Log ₁₀ final (Counts)	Log ₁₀ (Error)	Rel (%)	Com (%)
-1.30	0.050	5.36	0.09	89.46	53.1
-1.20	0.063	5.49	0.07	77.62	77.5
-1.10	0.079	5.48	0.09	89.06	84.0
-1.00	0.100	5.49	0.11	100.0	86.4
-0.90	0.126	5.60	0.12	100.0	88.5
-0.80	0.158	5.71	0.12	100.0	90.6
-0.70	0.200	5.69	0.14	100.0	91.5
-0.60	0.251	5.93	0.13	100.0	92.0
0.50	0.316	5.81	0.18	100.0	93.1
-0.40	0.398	5.78	0.22	100.0	94.0
-0.30	0.501	5.93	0.22	100.0	95.0
-0.20	0.631	5.95	0.25	100.0	95.6
-0.10	0.79	5.62	0.18	100.0	96.1
0.00	1.000	5.77	0.18	100.0	96.3
0.01	1.259	6.22	0.31	100.0	96.5

NEP counts, the *Spitzer* IRS peak-up counts (Teplitz et al. 2011), and the Pearson and SISSA models. All the source counts are in relatively good agreement and consistent with each other. Although the Pearson and SISSA evolutionary predictions peak at slightly different flux levels, both models are consistent with the observed counts (except at the faint end where they under predict compared to the IRS counts). However, it should be noted that the IRS counts were made over a very small area of 36 arcmin² and only 153 sources.

Fig. 24f shows both the IRAC Dark Field and ELAIS-N1 18 μ m counts with the *AKARI* NEP counts and the Pearson model. The counts presented here are in broad agreement with the NEP counts, given that the ELAIS-N1 L18W data were taken towards the end

Table 16. Final normalized differential source counts, $dN/dSS^{2.5}$, presented logarithmically as $mJy^{1.5} sr^{-1}$ for the L15 band in the IRAC Dark Field, with associated errors also presented logarithmically, reliability and completeness.

Log ₁₀ flux (/mJy)	Flux (/mJy)	Log ₁₀ final (Counts)	Log ₁₀ (Error)	Rel (%)	Com (%)
-0.90	0.126	6.04	0.08	95.06	63.0
-0.80	0.158	6.17	0.06	89.51	86.3
-0.70	0.200	6.30	0.07	93.47	90.3
-0.60	0.251	6.32	0.08	100.0	92.5
-0.50	0.316	6.19	0.11	100.0	93.6
-0.40	0.398	6.11	0.14	100.0	95.0
-0.30	0.501	6.29	0.13	100.0	95.7
-0.20	0.631	6.30	0.15	100.0	95.9
-0.10	0.794	6.15	0.22	100.0	96.3
0.00	1.000	5.70	0.18	100.0	96.6
0.20	1.585	5.99	0.18	100.0	97.7

Table 17. Final normalized differential source counts, $dN/dSS^{2.5}$, presented logarithmically as $mJy^{1.5} sr^{-1}$ for the L18W band in the IRAC Dark Field, with associated errors also presented logarithmically, reliability and completeness.

Log ₁₀ flux (/mJy)	Flux (/mJy)	Log ₁₀ final (Counts)	Log ₁₀ (Error)	Rel (%)	Com (%)
-0.80	0.158	6.21	0.08	100.0	58.5
-0.70	0.200	6.23	0.08	100.0	84.9
-0.60	0.251	6.14	0.10	100.0	89.4
-0.50	0.316	6.17	0.12	100.0	91.5
-0.40	0.398	5.86	0.19	100.0	93.3
-0.30	0.501	6.01	0.19	100.0	93.8
-0.20	0.631	5.93	0.25	100.0	94.8
-0.10	0.794	5.60	0.18	100.0	95.5
0.10	1.259	5.90	0.18	100.0	96.1

Table 18. Final normalized differential source counts, $dN/dSS^{2.5}$, presented logarithmically as $mJy^{1.5} sr^{-1}$ for the N4 band in the ELAIS-N1 field, with associated errors also presented logarithmically, reliability and completeness.

Log ₁₀ flux (/mJy)	Flux (/mJy)	Log ₁₀ final (Counts)	Log ₁₀ (Error)	Rel (%)	Com (%)
-2.00	0.010	4.71	0.06	100.0	61.7
-1.90	0.013	4.91	0.05	100.0	69.8
-1.80	0.016	5.08	0.05	100.0	73.9
-1.70	0.020	5.02	0.06	100.0	76.7
-1.60	0.025	5.20	0.06	100.0	80.6
-1.50	0.032	5.24	0.06	100.0	82.7
-1.40	0.040	5.19	0.08	100.0	85.3
-1.30	0.050	5.47	0.07	100.0	87.9
-1.20	0.063	5.30	0.09	100.0	89.9
-1.10	0.079	5.51	0.09	100.0	91.3
-1.00	0.100	5.26	0.14	100.0	92.4
-0.90	0.126	5.10	0.19	100.0	93.8
-0.80	0.158	5.33	0.18	100.0	94.8
-0.70	0.200	4.99	0.31	100.0	96.4
-0.60	0.251	4.84	0.18	100.0	96.9
-0.50	0.316	4.99	0.18	100.0	97.6
-0.40	0.398	5.14	0.18	100.0	98.0
-0.30	0.501	5.28	0.18	100.0	98.3
-0.10	0.794	5.58	0.18	100.0	98.7

Table 19. Final normalized differential source counts, $dN/dSS^{2.5}$, presented logarithmically as $mJy^{1.5} sr^{-1}$ for the S11 band in the ELAIS-N1 field, with associated errors also presented logarithmically, reliability and completeness.

Log ₁₀ flux (/mJy)	Flux (/mJy)	Log ₁₀ final (Counts)	Log ₁₀ (Error)	Rel (%)	Com (%)
−1.10	0.079	5.02	0.18	100.0	73.9
−1.00	0.100	5.28	0.14	100.0	86.7
−0.90	0.126	5.66	0.11	62.2	90.8
−0.80	0.158	5.74	0.12	78.8	91.9
−0.70	0.200	5.52	0.18	100.0	93.0
−0.60	0.251	5.96	0.13	100.0	94.2
−0.50	0.316	5.64	0.22	100.0	94.5
−0.40	0.398	5.18	0.18	100.0	94.9
−0.30	0.501	5.33	0.18	100.0	95.3
−0.10	0.794	6.11	0.25	100.0	95.5
0.10	1.259	6.23	0.31	100.0	96.2
0.20	1.585	6.08	0.18	100.0	96.3

Table 20. Final normalized differential source counts, $dN/dSS^{2.5}$, presented logarithmically as $mJy^{1.5} sr^{-1}$ for the L15 band in the ELAIS-N1 field, with associated errors also presented logarithmically, reliability and completeness.

Log ₁₀ flux (/mJy)	Flux (/mJy)	Log ₁₀ final (Counts)	Log ₁₀ (Error)	Rel (%)	Com (%)
−0.90	0.126	5.39	0.16	100.0	65.3
−0.80	0.158	6.12	0.08	96.8	72.4
−0.70	0.200	6.04	0.10	94.8	74.4
−0.60	0.251	6.13	0.11	94.1	76.3
−0.50	0.316	6.25	0.11	100.0	76.8
−0.40	0.398	6.17	0.14	100.0	77.4
−0.30	0.501	5.97	0.22	100.0	77.7
−0.20	0.631	5.99	0.25	100.0	78.6
−0.10	0.794	5.96	0.31	100.0	78.9
0.10	1.259	5.96	0.18	100.0	79.4
0.20	1.585	6.58	0.25	100.0	80.1

Table 21. Final normalized differential source counts, $dN/dSS^{2.5}$, presented logarithmically as $mJy^{1.5} sr^{-1}$ for the L18W band in the ELAIS-N1 field, with associated errors also presented logarithmically, reliability and completeness.

Log ₁₀ flux (/mJy)	Flux (/mJy)	Log ₁₀ final (Counts)	Log ₁₀ (Error)	Rel (%)	Com (%)
−0.90	0.126	5.86	0.11	89.0	52.1
−0.80	0.158	6.00	0.10	82.2	76.0
−0.70	0.200	6.38	0.07	97.8	86.2
−0.60	0.251	6.20	0.10	91.2	88.8
−0.50	0.316	5.92	0.15	100.0	91.1
−0.40	0.398	6.30	0.12	100.0	93.1
−0.30	0.501	6.00	0.19	100.0	94.0
−0.20	0.631	5.92	0.25	100.0	94.7
−0.10	0.794	6.20	0.22	100.0	95.0
0.00	1.000	6.04	0.31	100.0	96.2
0.10	1.259	5.89	0.18	100.0	96.6
0.30	1.996	6.48	0.31	100.0	97.4
0.60	3.981	6.63	0.18	100.0	98.2

Table 22. Final normalized differential source counts, $dN/dSS^{2.5}$, presented logarithmically as $mJy^{1.5} sr^{-1}$ for the N3 band in the ADF-S field, with associated errors also presented logarithmically, reliability and completeness.

Log ₁₀ flux (/mJy)	Flux (/mJy)	Log ₁₀ final (Counts)	Log ₁₀ (Error)	Rel (%)	Com (%)
−1.10	0.079	5.25	0.03	100.0	87.7
−1.00	0.100	5.67	0.02	100.0	91.1
−0.90	0.126	5.73	0.02	100.0	92.0
−0.80	0.158	5.71	0.03	100.0	93.4
−0.70	0.200	5.71	0.03	99.9	93.7
−0.60	0.251	5.75	0.04	100.0	94.1
−0.50	0.316	5.68	0.05	100.0	94.3
−0.40	0.398	5.72	0.06	100.0	95.2
−0.30	0.501	5.70	0.07	100.0	95.5
−0.20	0.631	5.51	0.10	100.0	96.1
−0.10	0.794	5.64	0.10	100.0	96.4
0.00	1.000	5.69	0.11	100.0	96.6
0.10	1.259	5.66	0.14	100.0	96.6
0.20	1.585	5.77	0.14	100.0	96.4
0.30	1.995	5.96	0.14	100.0	97.0
0.40	2.512	5.89	0.18	100.0	96.9
0.50	3.162	6.10	0.16	100.0	97.1
0.60	3.981	6.19	0.18	100.0	97.2
0.70	5.012	5.86	0.31	100.0	97.4
0.80	6.310	6.01	0.31	100.0	97.6
0.90	7.943	6.33	0.25	100.0	97.5
1.00	10.000	6.01	0.18	100.0	97.6
1.10	12.589	6.16	0.18	100.0	97.7
1.20	15.848	6.31	0.18	100.0	97.7

Table 23. Final normalized differential source counts, $dN/dSS^{2.5}$, presented logarithmically as $mJy^{1.5} sr^{-1}$ for the N4 band in the ADF-S field, with associated errors also presented logarithmically, reliability and completeness.

Log ₁₀ flux (/mJy)	Flux (/mJy)	Log ₁₀ final (Counts)	Log ₁₀ (Error)	Rel (%)	Com (%)
−1.30	0.050	5.23	0.02	100.0	88.1
−1.20	0.063	5.45	0.02	100.0	90.6
−1.10	0.079	5.43	0.0	100.0	91.7
−1.00	0.100	5.43	0.03	100.0	93.1
−0.90	0.126	5.39	0.03	100.0	93.7
−0.80	0.158	5.32	0.04	100.0	94.2
−0.70	0.200	5.31	0.05	100.0	95.1
−0.60	0.251	5.34	0.06	100.0	95.2
−0.50	0.316	5.14	0.09	100.0	95.6
−0.40	0.398	5.25	0.09	100.0	96.3
−0.30	0.501	5.10	0.13	100.0	96.6
−0.20	0.631	5.32	0.12	100.0	97.1
−0.10	0.794	5.43	0.13	100.0	97.2
0.00	1.000	5.35	0.16	100.0	97.5
0.10	1.259	5.35	0.19	100.0	97.7
0.20	1.585	5.80	0.14	100.0	98.2
0.30	1.995	5.43	0.25	100.0	98.1
0.40	2.512	5.70	0.22	100.0	98.1
0.50	3.162	5.25	0.18	100.0	98.2
0.60	3.981	5.70	0.31	100.0	98.3
0.70	5.012	5.85	0.31	100.0	98.3
1.00	10.000	6.30	0.31	100.0	98.4
1.40	25.119	6.60	0.18	100.0	98.4

Table 24. Final normalized differential source counts, $dN/dSS^{2.5}$, presented logarithmically as $mJy^{1.5} sr^{-1}$ for the S7 band in the ADF-S field, with associated errors also presented logarithmically, reliability and completeness.

Log ₁₀ flux (/mJy)	Flux (/mJy)	Log ₁₀ final (Counts)	Log ₁₀ (Error)	Rel (%)	Com (%)
-0.70	0.200	4.45	0.14	100.0	88.4
-0.60	0.251	5.41	0.05	100.0	96.8
-0.50	0.316	5.52	0.06	100.0	97.2
-0.40	0.398	5.67	0.06	100.0	97.5
-0.30	0.501	5.60	0.07	100.0	97.5
-0.20	0.631	5.60	0.09	100.0	97.6
-0.10	0.794	5.58	0.11	100.0	97.9
0.00	1.000	5.73	0.11	100.0	97.9
0.10	1.259	5.49	0.16	100.0	98.1
0.20	1.585	5.70	0.15	100.0	98.3
0.30	1.995	5.85	0.15	100.0	98.2
0.40	2.512	5.94	0.16	100.0	98.2
0.50	3.162	5.85	0.22	100.0	98.2
0.60	3.981	6.10	0.19	100.0	98.2
0.70	5.012	5.85	0.31	100.0	98.2
0.80	6.310	6.18	0.25	100.0	98.3
0.90	7.943	5.85	0.18	100.0	98.4
1.00	10.000	6.47	0.25	100.0	98.4
1.30	19.953	6.45	0.18	100.0	98.5
1.70	50.119	7.05	0.18	100.0	98.5

Table 25. Final normalized differential source counts, $dN/dSS^{2.5}$, presented logarithmically as $mJy^{1.5} sr^{-1}$ for the S11 band in the ADF-S field, with associated errors also presented logarithmically, reliability and completeness.

Log ₁₀ Flux (/mJy)	Flux (/mJy)	Log ₁₀ Final (Counts)	Log ₁₀ (Error)	Rel (%)	Com (%)
-0.80	0.158	4.98	0.12	94.51	54.0
-0.70	0.200	5.30	0.07	95.52	85.3
-0.60	0.251	5.38	0.06	98.34	92.0
-0.50	0.316	5.99	0.03	100.0	92.9
-0.40	0.398	6.12	0.03	100.0	93.6
-0.30	0.501	6.28	0.03	99.49	93.7
-0.20	0.631	6.18	0.05	100.0	93.7
-0.10	0.794	6.29	0.05	100.0	94.2
0.00	1.000	6.35	0.05	100.0	94.2
0.10	1.259	6.30	0.07	100.0	94.5
0.20	1.585	6.19	0.09	100.0	94.7
0.30	1.995	6.11	0.12	100.0	94.7
0.40	2.512	6.11	0.14	100.0	94.8
0.50	3.162	6.30	0.13	100.0	95.0
0.60	3.981	6.19	0.18	100.0	95.0
0.70	5.012	6.34	0.18	100.0	95.0
0.80	6.310	6.31	0.22	100.0	94.9
0.90	7.943	6.16	0.31	100.0	95.2
1.00	10.000	6.61	0.22	100.0	95.1

of Phase 2 and therefore were severely affected by Earthshine, which is likely to be responsible for the large scatter. There is some hint that the counts fall off steeper than the evolutionary model predicts but given the large uncertainties this is not well constrained.

A small disparity in source counts from two different deep fields is believed to be due to cosmic variance (Somerville et al. 2004), the uncertainty in the number of galaxies in a given volume density, caused by large-scale density fluctuations. The percentage of cosmic

Table 26. Final normalized differential source counts, $dN/dSS^{2.5}$, presented logarithmically as $mJy^{1.5} sr^{-1}$ for the L15 band in the ADF-S field, with associated errors also presented logarithmically, reliability and completeness.

Log ₁₀ flux (/mJy)	Flux (/mJy)	Log ₁₀ final (Counts)	Log ₁₀ (Error)	Rel (%)	Com (%)
-0.40	0.398	4.72	0.22	100.0	58.6
-0.30	0.501	5.45	0.09	100.0	97.1
-0.20	0.631	6.01	0.05	100.0	98.3
-0.10	0.794	5.95	0.07	100.0	98.4
0.00	1.000	5.93	0.08	100.0	98.6
0.10	1.259	5.90	0.10	100.0	98.9
0.20	1.585	5.57	0.18	100.0	99.0
0.30	1.995	5.42	0.25	100.0	98.8
0.40	2.512	5.79	0.19	100.0	99.1

variance is greater for deep, narrow fields, e.g. the IRAC Dark Field, ELAIS-N1 and NEP. A discrepancy in the SISSA model and the shorter source counts could be due to the fact that elliptical galaxies are not fully modelled. At high- z the SISSA model includes a term for the evolution of proto-spheroid galaxies, the progenitors to elliptical galaxies, but they do not fully model the evolution of proto-spheroids to ellipticals. Also at low- z there is no specific term for elliptical galaxies, and there are no discussion about the formation of ellipticals through major merger of spiral galaxies. Thus, including the evolution of elliptical galaxies in the SISSA model should increase the predicted source counts. The biggest increase would be expected at the shorter wavelengths, where the contribution from the older stellar population is significant. This could explain the discrepancy between the SISSA model and the source counts at 7 μm .

Overall, a combination of the deep IRAC Dark Field and ELAIS-N1, and the shallower ADF-S fields covers a large range in flux density from $0.1 < S < 10 mJy$. Over this range, both evolutionary models fit the majority of the source counts well. There is evidence that in the mid-short infrared bands (7, 11 μm) that some modification is needed in the models. At these wavelengths, the SISSA model performs slightly better than the Pearson model. The inconsistencies may be due to incorrect stellar subtraction on the counts, or may suggest incorrect modelling of stellar populations, e.g. thermally pulsating asymptotic giant branch (TP-AGB) stars.

7 INVESTIGATION OF AKARI COLOURS

In this section, the colour-colour diagrams in the mid infrared, specifically *AKARI* N4, S11, L15 and L18W, are investigated. Most of the work using mid-infrared colour-colour diagrams to differentiate between AGN and star-forming galaxies has been performed using the *Spitzer*/IRAC and MIPS filters (Lacy et al. 2004; Stern et al. 2005; Donley et al. 2012). There is some published work on using the AKARI/IRC mid-infrared filters to separate AGN-dominated galaxies and star-forming galaxies (Hanami et al. 2012). Investigation of the *AKARI* colours was mainly performed to trace the PAH emission bands, which was used for galaxy separation and to calculate star formation rate. The study of PAH in galaxy separation may not always work, as PAH features can be suppressed in star-forming galaxies, and in some cases, AGNs are known to have PAH emission (Laurent et al. 2000; Murata et al. 2014b).

Table 27. The first 10 lines of the *AKARI*/IRAC Dark Field galaxy catalogue. The complete catalogue is available online.

RA	DEC	N4 flux (/mJy)	N4 error (/mJy)	S11 flux (/mJy)	S11 error (/mJy)	L15 flux (/mJy)	L15 error (/mJy)	L18W flux (/mJy)	L18W error (/mJy)
264.96	69.08	0.027	0.0014	0.16	0.0069	0.11	0.016	0.16	0.018
264.99	69.08	0.036	0.0016	0.16	0.0070	0.15	0.014	0.20	0.019
265.07	69.08	0.030	0.0015	0.048	0.0046	0.16	0.012	0.15	0.018
265.08	69.03	0.069	0.0022	0.23	0.0077	0.21	0.015	0.25	0.020
265.08	69.04	0.030	0.0015	0.081	0.0054	0.20	0.015	0.14	0.017
265.02	69.07	0.045	0.0019	0.058	0.0050	0.18	0.014	0.26	0.020
265.05	69.06	0.038	0.0017	0.10	0.0059	0.21	0.015	0.26	0.020
265.03	69.06	0.054	0.0020	0.052	0.0048	0.14	0.014	0.27	0.020
265.02	69.07	0.098	0.0027	0.058	0.0049	0.18	0.015	0.13	0.017
264.88	69.05	0.040	0.0017	0.030	0.0044	0.087	0.012	0.14	0.017

Due to the fact that the *AKARI* mid-infrared filters were designed to study the PAH features, which are prominent in star-forming and AGN composite objects, star-forming and spiral galaxies, and to a lesser extent in AGN; the tracks of these types of galaxies cover much of the *AKARI* colour–colour space. Thus, many different galaxy types lie in the same region of the *AKARI* colour–colour plots. This is a feature seen in all *AKARI* colour–colour plots, and an indication that the *AKARI* colour–colour space is not ideally suited for galaxy separation.

Fig. 25 shows two *AKARI* colour–colour plots, with a starburst (green) and AGN (red) track made from SED templates of Berta et al. (2013), and *AKARI*/IRAC Dark Field and ELAIS-N1 sources. In the mid-infrared, at $z < 2$, the starburst track is dominated by PAH features, as the features travel through the different filters. It is the PAHs that are mainly causing the changes in track angle. On the *AKARI* colour–colour diagrams, the AGN tracks cover a smaller area of the plot than the starburst track. This is due to the fact that PAH emission tends to be suppressed in AGN-dominated galaxies, due to the intense radiation from the AGN, thus the AGN tracks do not have as prominent PAH features travelling through the filters, and causing the tracks to move around the diagram to the same extent as for the starburst track. The changes in direction of the starburst track can be explained by the PAH features. Fig. 25a shows S11/N4 against L18W/S11. At $z \sim 0.2$, the S11/N4 flux ratio decreases, while the L18W/S11 flux ratio increases. This is due to the $7.7 \mu\text{m}$ PAH feature leaving the S11 filter at increasing redshift. Fig. 25b shows S11/N4 against L15/S11. The sharp decrease in the flux ratio L15/S11 and only a small increase in the S11/N4 flux ratio at the $z \sim 1.4$ is due to the $6.2 \mu\text{m}$ PAH feature leaving the L15 filter.

It was investigated whether AGN-dominated galaxies could be separated from starburst galaxies by just using the IRAC Dark Field and ELAIS-N1 *AKARI* colours. Figs 25a and b show colour–colour diagrams of the *AKARI* filters. The starburst and the AGN track go from $0 < z < 2$. As the AGN track clearly occupies a different region from the starburst track, for this range of redshifts an AGN selection area on the colour–colour plot has been identified, i.e. the area around the AGN track. For the galaxies in these two plots, ~ 75 percent have $z < 2$, so this is not an unreasonable redshift cut-off. As can be seen in Fig. 25, the galaxies do not just populate the starburst and the AGN tracks, but are also found in regions between, indicating that many of the sources are composite objects. This indicates that to reliably confirm galaxy type, SED fitting is required. This investigation has only just four of the nine *AKARI* filters. An investigation including filters not observed by the IRAC Dark Field and

ELAIS-N1 (e.g. the S9W filter) may find further AGN selection criteria.

8 CONCLUSIONS

A new toolkit for observations made with the *AKARI* IRC instrument has been presented that is specifically optimized for the data analysis of extragalactic fields. The main differences between the optimized toolkit and the archival pipeline are the removal of hot pixels, creation of noise images, distortion correction, Earthshine light correction, astrometry correction and the masking of artefacts.

This optimized toolkit was applied to three *AKARI* example test fields: the narrow-deep early to mid-Phase 2 IRAC Dark Field, the narrow-deep late-Phase 2 ELAIS-N1 field and the wide-shallow ADF-S field. These fields were selected on the basis of difficulty of reduction using the archival pipeline. Source catalogues and completeness plus reliability-corrected source counts were produced for the *AKARI* bands from 3 to $18 \mu\text{m}$ spanning the wavelength desert between the *Spitzer* IRAC and MIPS instruments.

The 4, 11, 15 and $18 \mu\text{m}$ *AKARI* colours have been investigated, and AGN selection criteria have been found for galaxies $z < 2$. When plotting the *AKARI*/IRAC Dark Field and ELAIS-N1 sources on colour–colour plots, many objects were identified as star-forming and AGN composite objects.

The source count results presented in this paper are in broad agreement with the previously published results from *AKARI* surveys and *Spitzer* surveys with the IRAC instrument and IRS peak-up observations. We do, however, also find discrepancies at brighter fluxes (in the ADF-S) in some instances that we attribute to problems with the stellar subtraction in either the *AKARI* or IRAC data.

The observed source counts were also compared with the galaxy evolutionary models of Pearson (2005), Pearson & Khan (2009) and Cai et al. (2013). We find that no single evolutionary model can fit all the wavebands simultaneously. The models are in good agreement with the counts at wavelengths longer than $11 \mu\text{m}$ but have difficulties at shorter wavelengths. This could be due to incorrect stellar subtraction in the source counts, or incorrect modelling of stellar populations.

Further data reduction of other extragalactic fields in the *AKARI* data archive using the optimized toolkit is expected to constrain the evolutionary models further and will be presented in future work.

ACKNOWLEDGEMENTS

The *AKARI* Project is an infrared mission of the Japan Space Exploration Agency (JAXA) Institute of Space and Astro-nautical

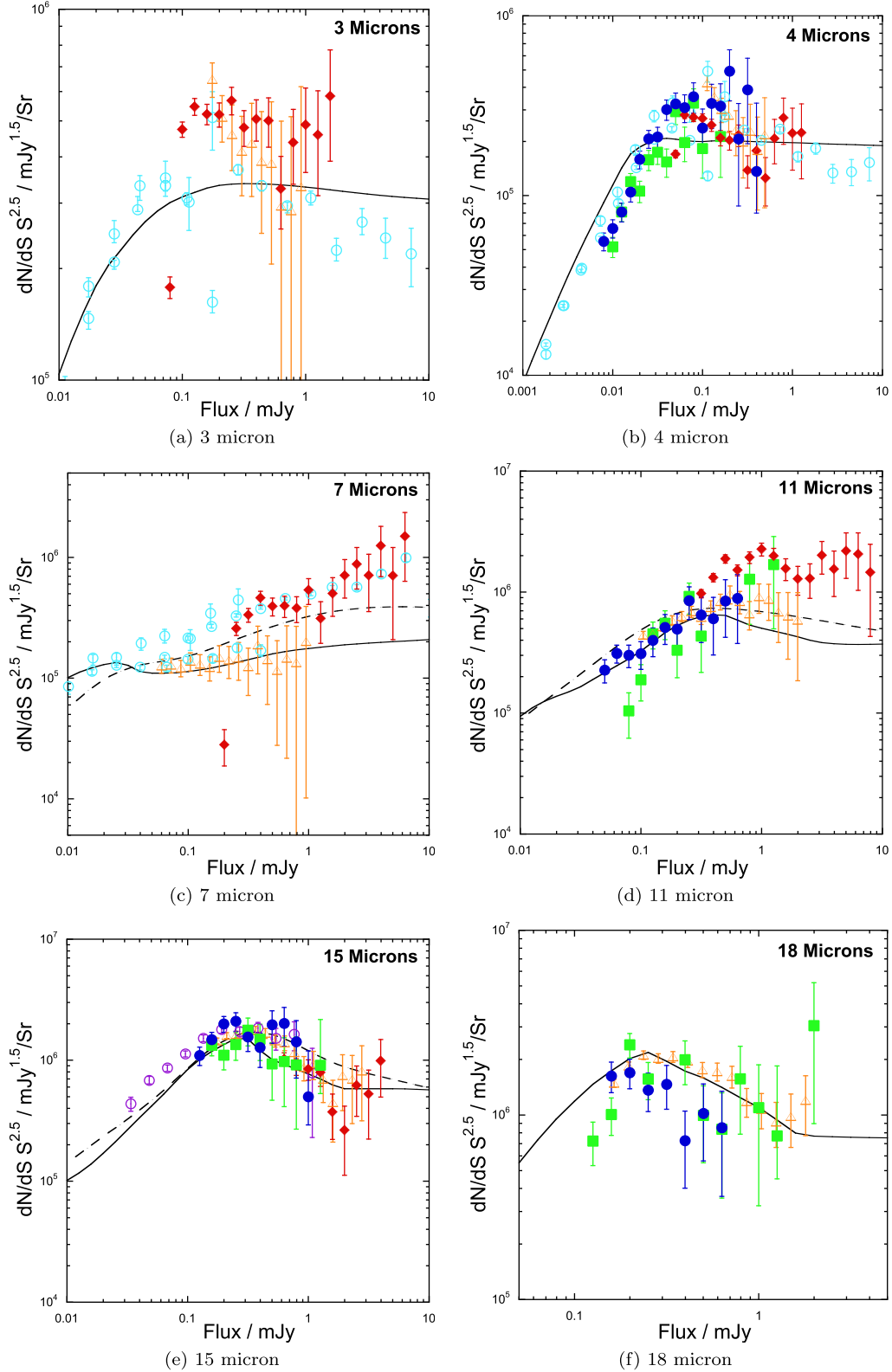


Figure 24. Comparison of the AKARI/IRAC Dark Field, ELAIS-N1 and ADF-S source counts from this work, with the source counts from the AKARI/NEP survey and *Spitzer*/IRAC and *Spitzer*/IRS surveys. The IRAC Dark Field counts are shown as dark blue circles, ELAIS-N1 number counts as green squares, and the ADF-S counts as red diamonds. The AKARI/NEP number counts are shown as open orange triangles (Murata et al. 2014a), the *Spitzer*/IRAC counts as open cyan circles (Fazio et al. 2004) and the *Spitzer*/IRS as open purple circles (Teplitz et al. 2011). The SISSA model is shown as a dashed line. The Pearson model is shown as a solid line, the grey line is the contribution of normal type galaxies, the magenta line is the contribution of elliptical-type galaxies, the red line is the contribution of star-forming galaxies, the cyan line is the contribution of LIRGs, the blue line is the contribution of ULIRGs and the green line is the contribution of AGN.

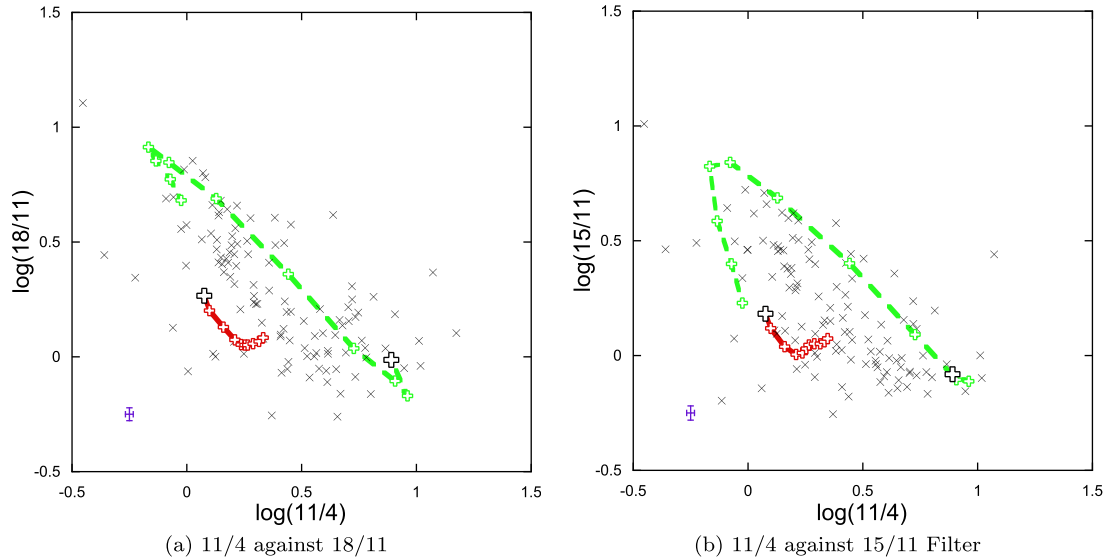


Figure 25. Colour–colour diagrams of the AKARI N4, S11, L15 and L18W filters. The black crosses are the ELAIS-N1 and IRAC Dark Field galaxy colours, the starburst track is in the dashed green line and the AGN track is in solid red line. The tracks in figures (a) and (b) have been cut at $z = 2$. $z = 0$ is marked by a larger cross. An example error for the galaxy flux is shown as the purple error bars in the lower left corner.

Science (ISAS), and is carried out with the participation of mainly the following institutes: Nagoya University, The University of Tokyo, National Astronomical Observatory Japan, The European Space Agency (ESA), Imperial College London, University of Sussex, The Open University (UK), University of Groningen/SRON (The Netherlands), Seoul National University (Korea). The far-infrared detectors were developed under collaboration with The National Institute of Information and Communications Technology.

The authors would like to acknowledge the STFC Doctoral training grant ST/K502212/1 and support from the Open University.

Helen Davidge would also like to thank the Japan Society for the Promotion of Science for financial support on the JSPS Summer Programme 2015.

REFERENCES

- Arimatsu K. et al., 2011, *PASP*, 123, 981
 ASTRO-F User Support Team., 2005, Version 3.2
 Basilakos S. et al., 2002, *MNRAS*, 331, 417
 Berta S. et al., 2013, *AAP*, 551, A100
 Bertin E., Arnouts S., 1996, *A&AS*, 117, 393
 Blain A. W., Longair M. S., 1993, *MNRAS*, 264, 509
 Cai Z.-Y. et al., 2013, *ApJ*, 768, 21
 Chary R. et al., 2004, *ApJS*, 154, 80
 Ciliegi P. et al., 1999, *MNRAS*, 302, 222
 Clements D. L. et al., 2011, *MNRAS*, 411, 373
 Donley J. L. et al., 2012, *ApJ*, 748, 142
 Egusa F., Usui F., Murata K., Yamashita T., Yamamura I., Onaka T., 2016, *PASJ*, 68, 19
 Ellis R., 1987, in *Proc. IAU Symp. 124, Observational Cosmology*. D. Reidel Publishing Co., Dordrecht, p. 367
 Fazio G. G. et al., 2004, *ApJS*, 154, 39
 Franceschini A., Toffolatti L., Mazzei P., Danese L., de Zotti G., 1991, *AAS*, 89, 285
 Gehrels N., 1986, *ApJ*, 303, 336
 Granato G. L., De Zotti G., Silva L., Bressan A., Danese L., 2004, *ApJ*, 600, 580
 Hanami H. et al., 2012, *PASJ*, 64, 70
 Hatsukade B. et al., 2011, *MNRAS*, 411, 102
 Ishihara D. et al., 2010, *A&A*, 514, A1
 Kawada M. et al., 2007, *PASJ*, 59, 389
 Kessler M. et al., 1996, *A&A*, 315, L27
 Krick J. E. et al., 2009, *ApJS*, 185, 85
 Lacy M. et al., 2004, *ApJS*, 154, 166
 Laurent O., Mirabel I. F., Charmandaris V., Gallais P., Madden S. C., Sauvage M., Vigroux L., Cesarsky C., 2000, *A&A*, 359, 887
 Lorente R. et al., 2007, *AKARI IRC Data User Manual*, version 1.3
 Maddox S. J., Efstathiou G., Sutherland W. J., Loveday J., 1990, *MNRAS*, 243, 692
 Manners J. C. et al., 2003, *MNRAS*, 343, 293
 Markwardt C. B., 2009, in *Bohlender D. A., Durand D., Dowler P., eds, ASP Conf. Ser. Vol. 411, Astronomical Data Analysis Software and Systems XVIII*. Astron. Soc. Pac., San Francisco, p. 251
 Matsuura S. et al., 2011, *ApJ*, 737, 2
 Matute I. et al., 2002, *MNRAS*, 332, L11
 McMahon R. G. et al., 2001, *New Astron. Rev.*, 45, 97
 Mortara L., Fowler A., 1981, in *Proc. SPIE Conf. Ser. Vol. 290, Solid State Images for Astronomy*. SPIE, Bellingham, p. 28
 Murakami H. et al., 2007, *PASJ*, 59, S369
 Murata K. et al., 2013, *A&A*, 559, A132
 Murata K., Pearson C. P., Goto T., Kim S. J., Matsuhara H., Wada T., 2014a, *MNRAS*, 444, 2346
 Murata K. et al., 2014b, *A&A*, 566, A136
 Oliver S. et al., 2000, *MNRAS*, 316, 749
 Oliver S. J. et al., 2012, *MNRAS*, 424, 1614
 Onaka T. et al., 2007, *PASJ*, 59, 401
 Pearson C., 2005, *MNRAS*, 358, 1417
 Pearson C. P., Khan S., 2009, *MNRAS*, 358, L11
 Pearson C., Rowan-Robinson M., 1996, *MNRAS*, 283, 174
 Pearson C. P. et al., 2010, *A&A*, 514, A9
 Rowan-Robinson M., 1967, *Nature*, 216, 1289
 Scott K. S. et al., 2010, *ApJS*, 191, 212
 Skrutskie M. F. et al., 2006, *AJ*, 131, 1163
 Somerville R. S., Lee K., Ferguson H. C., Gardner J. P., Moustakas L. A., Giavalisco M., 2004, *ApJ*, 600, L171
 Stern D. et al., 2005, *ApJ*, 631, 163
 Tanabé T., Sakon I., Cohen M. et al., 2008, *PASJ*, 60, 375
 Teplitz H. I. et al., 2011, *AJ*, 141, 1
 Tsumura K., Wada T., 2011, *PASJ*, 63, 755
 Väisänen P. et al., 2002, *MNRAS*, 337, 1043

Valiante E. et al., 2010, ApJS, 191, 222
 van Dokkum P. G., 2001, PASP, 113, 1420
 Werner M. W. et al., 2004, ApJS, 154, 1
 White G. J. et al., 2012, MNRAS, 427, 1830
 Wright E. L. et al., 2010, AJ, 140, 1868
 Yamamura I., Makiuti S., Ikeda N., Fukuda Y., Oyabu S., Koga T.,
 White G. J., 2010, AKARI-FIS Bright Source Catalogue Release
 note Version 1.0, <http://www.ir.isas.jaxa.jp/ASTRO-F/Observation/PSC/Public/>

SUPPORTING INFORMATION

Supplementary data are available at [MNRAS](#) online.

AKARI_IRAC_Dark_Field_Galaxy_Catalogue.txt

AKARI_ELAIS_N1_Galaxy_Catalogue.txt

AKARI_ADF-S_Galaxy_Catalogue.txt

Please note: Oxford University Press is not responsible for the content or functionality of any supporting materials supplied by the authors. Any queries (other than missing material) should be directed to the corresponding author for the article.

APPENDIX: DISTORTION POLYNOMIALS

The distortion correction polynomials used in the optimized toolkit.

N2 filter

x_{ij}	0	1	2
0	−5.83	0.00190	0.0000111
1	1.02	0.0000372	−0.0000000809
2	−0.0000106	0.00000000946	0.000000000218

y_{ij}	0	1	2
0	5.53	0.986	0.0000157
1	−0.0140	−0.0000182	0.0000000933
2	0.0000151	0.0000000286	−0.00000000217

N3 filter

x_{ij}	0	1	2
0	−3.35	0.00356	0.00000682
1	1.02	0.0000157	−0.00000000996
2	−0.0000131	0.0000000653	−0.000000000155

y_{ij}	0	1	2
0	5.55	0.985	0.0000183
1	−0.0117	−0.0000119	0.0000000434
2	0.0000101	0.00000000766	−0.000000000696

N4 filter

x_{ij}	0	1	2
0	−4.01	0.00472	0.00000255
1	1.02	0.0000165	0.00000000153
2	−0.00000648	0.0000000232	−0.0000000000770

y_{ij}	0	1	2
0	2.79	0.984	0.0000210
1	−0.0117	−0.0000182	0.0000000562
2	0.0000121	0.0000000243	−0.000000000123

S7 filter

x_{ij}	0	1	2
0	−1.64	−0.00206	0.0000597
1	0.987	0.000424	−0.00000127
2	0.0000754	−0.00000124	0.00000000372

y_{ij}	0	1	2
0	1.186	1.03	−0.0000342
1	−0.0150	−0.0000464	0.000000140
2	0.00000631	−0.000000149	0.000000000357

S9W filter

x_{ij}	0	1	2
0	−6.03	0.0116	0.0000231
1	1.02	0.0000693	−0.000000256
2	−0.0000120	−0.000000104	0.000000000476

y_{ij}	0	1	2
0	0.930	1.03	−0.0000246
1	−0.0141	−0.0000357	0.0000000382
2	−0.00000399	−0.0000000922	0.000000000486

S11 filter

x_{ij}	0	1	2
0	−3.71	−0.0265	0.000167
1	0.994	0.000635	−0.00000234
2	0.0000643	−0.00000219	0.00000000804

y_{ij}	0	1	2
0	−2.99	1.06	−0.000186
1	0.00653	−0.000683	0.00000332
2	−0.0000683	0.00000231	−0.0000000116

L15 filter

x_{ij}	0	1	2
0	8.06	0.00799	− 0.0000285
1	0.949	− 0.000125	0.000000418
2	− 0.000101	− 0.000000206	0.000000000793

y_{ij}	0	1	2
0	− 2.09	1.01	0.00000684
1	− 0.0111	0.000205	− 0.000000563
2	0.0000543	− 0.00000124	0.00000000396

L18W filter

x_{ij}	0	1	2
0	7.38	0.0125	− 0.0000459
1	0.951	− 0.000221	0.000000677
2	− 0.000125	0.000000662	− 0.00000000172

y_{ij}	0	1	2
0	− 2.96	1.01	− 0.00000412
1	0.00101	− 0.0000439	0.000000199
2	− 0.00000396	0.000000152	− 0.000000000453

L24 filter

x_{ij}	0	1	2
0	8.25	− 0.00220	0.00000134
1	0.933	− 0.0000637	0.000000380
2	− 0.0000709	0.000000267	− 0.00000000142

y_{ij}	0	1	2
0	− 0.178	1.012	0.0000161
1	− 0.00356	0.0000791	− 0.000000312
2	0.0000135	− 0.000000220	0.000000000965

This paper has been typeset from a $\text{\TeX}/\text{\LaTeX}$ file prepared by the author.